

# Time-dependent friction effects on vibrational infrared frequencies and line shapes of liquid water

Florian N. Brünig, Otto Geburtig, Alexander von Canal, Julian Kappler, and Roland R. Netz\*  
*Freie Universität Berlin, Germany*

From ab initio simulations of liquid water, the time-dependent friction functions and time-averaged non-linear effective bond potentials for the OH stretch and HOH bend vibrations are extracted. The obtained friction exhibits adiabatic contributions at and below the vibrational time scales, but also much slower non-adiabatic contributions, reflecting homogeneous and inhomogeneous line broadening mechanisms, respectively. Compared to the gas phase, hydration softens both stretch and bend potentials, which by itself would lead to a red-shift of the corresponding vibrational bands. In contrast, non-adiabatic friction contributions cause a spectral blue shift. For the stretch mode, the potential effect dominates and thus a significant red shift when going from gas to the liquid phase results. For the bend mode, potential and non-adiabatic friction effects are of comparable magnitude, so that a slight blue shift results, in agreement with well-known but puzzling experimental findings. The observed line broadening is shown to be roughly equally caused by adiabatic and non-adiabatic friction contributions for both, the stretch and bend modes in liquid water. Thus, the understanding of infrared vibrational frequencies and line shapes is considerably advanced by the quantitative analysis of the time-dependent friction that acts on vibrational modes in liquids.

## I. INTRODUCTION

The OH stretch band in liquid water is significantly red-shifted and broadened compared to the gas phase spectrum, while the HOH bend frequency is in fact slightly blue-shifted when going from gas to the liquid phase [1]. The broadening of the OH stretch band in liquid water is typically rationalized by a combination of homogeneous and inhomogeneous effects [2, 3]. Inhomogeneous line broadening is associated with different hydrogen-bonding environments of individual OH bonds, which in the limit when the hydrogen-bonding pattern changes more slowly than the OH vibrational period and in the presence of non-linearities in the OH bond potential, produce vibrational frequencies that vary over time [4–6]. Homogeneous line broadening reflects the fast coupling of OH bonds to their neighboring water molecules, mostly via hydrogen bonding, which reduces the vibrational life time since the vibrational energy is quickly transported to neighboring molecules and thus dissipated into collective modes. Indeed, the vibrational life time of the OH stretch is very short (of the order of 190 fs [7, 8]) and thus only 19 times longer than the OH-stretch vibrational period itself (of the order of 10 fs). The experimentally observed red shift of the OH stretch band is usually rationalized by strong hydrogen bonding in liquid water, which extends and thereby softens the OH bond [2, 3] (in fact, the relationship between the hydrogen-bond strength, the OH bond length and the red shift of the stretch band has been amply and partly controversially discussed in literature [5, 9–11]). According to such reasoning, the rather small frequency shift of the water bending mode when going from gas to liquid water could be argued to imply that the bond angle potential is only weakly perturbed by the

liquid water environment and thus that the coupling of bend vibrations to the hydration environment is weak. This interpretation is puzzling though, since the vibrational life time of the water bending mode in liquid water is rather short (around 170 fs [12, 13]) and thus only 8.5 times longer than the vibrational period of 20 fs, an even smaller ratio than for the stretch mode. The short bend vibrational life time reflects quick energy dissipation into librational modes [14–16], which in turn can be rationalized by efficient multiphonon energy relaxation based on the excitation of librational overtones in liquids [17]. In this paper, we address the puzzle posed by the different line shifts of the water stretch and bend modes by analyzing the vibrational water dynamics in terms of the time-averaged non-linear bond potentials (as a function of the bond length for the OH stretch and the bond angle for the HOH bend) and the time-dependent friction functions, which are extracted from extensive ab initio Molecular Dynamics (aiMD) simulations for 256 H<sub>2</sub>O molecules. In particular, we show that the slight blue shift of the water bend mode when going from gas to the liquid phase is not caused by a stiffening of the bend potential [1], but rather by the time dependence of the friction acting on bending vibrations.

Time- or, equivalently, frequency-dependent friction arises whenever the dynamics of a many-particle system is described in a low-dimensional reaction-coordinate space [18–24] and its relevance for infrared (IR) spectra was clearly demonstrated in the past [25–30]. All friction contributions that decay faster or similarly as the vibrational period stem from adiabatic solvent degrees of freedom and account for dissipation into intra- and intermolecular degrees of freedom (including vibrational overtones) [31–34], these friction contributions dominate the vibrational energy relaxation and lead to homogeneous line broadening. Friction contributions that decay much slower than the vibrational time scale describe the slowly changing non-adiabatic hydration environment and in conjunction

\* rnetz@physik.fu-berlin.de

with non-linear bond potentials induce inhomogeneous line broadening, as our results explicitly demonstrate. Of course, there is no clear-cut separation between adiabatic and non-adiabatic solvent relaxation modes [35–38], prompting for a time-scale bridging framework to treat the dynamic coupling of molecular vibration modes and their environment. In fact, the frequency-dependent friction function, which appears in the generalized Langevin equation (GLE), is the appropriate framework to account for all these effects, with the only drawback that nuclear quantum effects can at the current level of the formalism not be included. Only recent improvements of the extraction methods [39] allow to obtain these time-dependent friction functions from aiMD simulations and with high enough accuracy: this we self-consistently demonstrate by predicting spectra from the GLE that are virtually indistinguishable from the spectra directly obtained from aiMD simulations.

We find that the liquid environment in fact significantly softens the time-averaged bond potentials, and it does so quite similarly for the stretch and bend modes. Neglecting the frequency dependence of the friction, both stretch and bend bands would thus be expected to be red-shifted by comparable amounts when going from gas to the liquid phase, in stark contrast to the experimental finding [1]. It turns out that non-harmonic bond-potential effects are rather unimportant for the band position and thus cannot explain this puzzling finding. Likewise, frequency-independent friction shifts the bands insignificantly and only increases the line width, in agreement with expectations [4]. In contrast, the frequency dependence of the friction is crucial and leads, in conjunction with non-linearities in the bond potentials, not only to inhomogeneous line broadening but also gives rise to pronounced blue shifts for both stretch and bend bands. The mechanism for this blue shift is very general [25], as we analytically demonstrate. The compensation of the potential red shift and the friction blue shift is incomplete for the stretch band but almost perfect for the bend band, so the stretch band exhibits a significant net red shift from gas to liquid, while the bend band only shows a slight blue shift in both experiments and simulations. The absence of a significant frequency shift of the bend mode does by no means imply that bend vibrations couple less to their environment than stretch vibrations (as has been demonstrated previously [14–16]): rather, it is the balance of the potential and friction contributions to the line shift, which both are caused by interactions with the liquid environment, that is different for the stretch and bend bands. We conclude that the coupling of water stretch and bend vibrations to other intra- and intermolecular degrees of freedom, as quantified by the time-averaged bond potentials and friction functions, is of similar strength, which explains their similar vibrational life times, although their frequency shifts are rather different, which we rationalize by a subtle difference of the compensatory potential and friction effects. The spectral blue shift due to frequency-dependent friction is a

very general mechanism; it transpires that the concept of frequency-dependent friction is important for advancing the understanding of vibrational spectroscopy.

## II. SYSTEM, SPECTRA AND MODEL

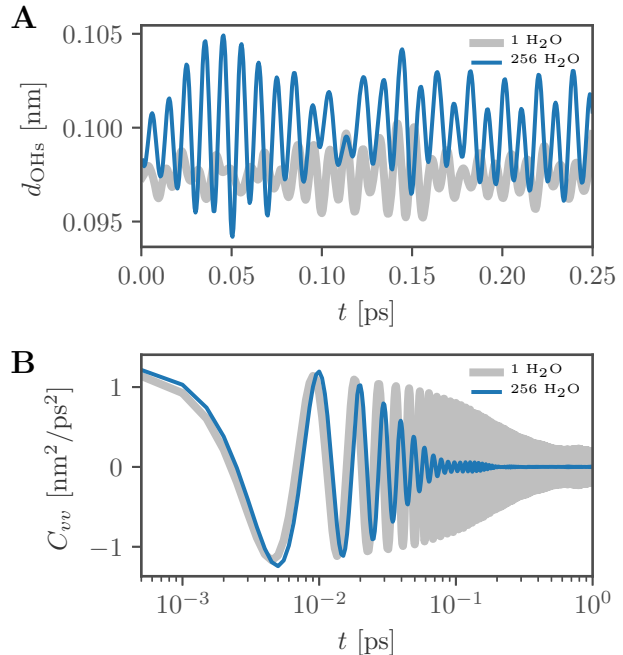


FIG. 1. **A:** Trajectory of the OH bond length, averaged over both OH bonds in a single water molecule, from ab initio Molecular Dynamics (aiMD) simulations of one H<sub>2</sub>O in the gas phase (grey line) and for 256 H<sub>2</sub>O in the liquid phase (blue line), both at 300 K. **B:** Corresponding velocity autocorrelation functions.

We primarily analyze aiMD simulations of 256 H<sub>2</sub>O (and D<sub>2</sub>O for comparison) molecules in the liquid phase at 300 K that neglect nuclear quantum effects. Fig. 1A compares the trajectories of the mean OH bond length of a single H<sub>2</sub>O molecule in liquid H<sub>2</sub>O (blue line) and in the gas phase (grey line), both at 300 K (see Methods for simulation details). The increase of the mean and the variance of the bond length in the liquid phase compared to the gas phase is clearly visible, which reflects the shift and softening of the OH bond potential due to hydrogen bonding in the liquid phase. The slow fluctuations of the oscillation amplitude reflect vibrational energy relaxations that occur over about 100 fs in the liquid phase (pure dephasing due to fluctuations of the vibrational frequency [40, 41] is not easily visible in the time domain). Similarly, the bond-length velocity autocorrelation function (VACF) in fig. 1B demonstrates a significantly faster decay and thus a decreased vibrational life time in the liquid phase. Although the OH-stretch absorption spectrum is (apart from electronic and collective effects) straightforwardly

related to the OH bond-length VACF via Fourier transformation, it turns out that only the careful analysis in terms of the GLE reveals the mechanisms that determine the OH-stretch vibration frequency and line shape.

Linear IR spectroscopy experiments measure the absorbed power of light at angular frequency  $\omega = 2\pi f$ , which is proportional to the imaginary part of the dielectric susceptibility  $\tilde{\chi}''(\omega)$ . Linear-response theory relates  $\tilde{\chi}''(\omega)$  to the total dipole-moment autocorrelation (see SI section I), allowing IR spectra to be calculated from equilibrium simulations [44, 45]. Fig. 2A compares the IR spectrum from aiMD simulations of liquid H<sub>2</sub>O (grey solid line) and D<sub>2</sub>O (blue solid line) with corresponding experimental data (grey and blue broken lines, respectively). One discerns the stretch band (around 3300 cm<sup>-1</sup> for H<sub>2</sub>O and 2400 cm<sup>-1</sup> for D<sub>2</sub>O in the aiMD results) and the bend band (at 1650 cm<sup>-1</sup> for H<sub>2</sub>O and 1200 cm<sup>-1</sup> for D<sub>2</sub>O). The librational band is produced by a large number of different intermolecular vibrational modes [46] that are dominated by rotational vibrations of water molecules in their hydrogen-bond environment (around 700 cm<sup>-1</sup> for H<sub>2</sub>O and 550 cm<sup>-1</sup> for D<sub>2</sub>O) and by translational vibrations of water molecules against each other around 200 cm<sup>-1</sup> for both H<sub>2</sub>O and D<sub>2</sub>O. The agreement between aiMD simulations, which fully account for electronic and nuclear polarizations, and experimental spectra is good, which suggests that the chosen simulation method is well suited for modeling IR spectra, although the agreement is known to be partly due to a cancellation of approximations in the employed density functional theory (DFT) and the neglect of nuclear quantum effects [47, 48]. However, the interplay of potential and frequency-dependent friction effects we tackle in this paper presumably is not modified by nuclear quantum effects in a fundamental way, so that the conclusions we draw should remain valid even beyond the Born-Oppenheimer approximation.

Fig. 2B compares simulated liquid H<sub>2</sub>O (grey) and single H<sub>2</sub>O (blue solid line) spectra at 300 K. The single water spectrum shows sharp peaks which perfectly coincide with the normal mode frequencies of a single water molecule (vertical dotted lines, computed on the same DFT level as the aiMD simulations) at 1607 cm<sup>-1</sup>, 3675 cm<sup>-1</sup> and 3772 cm<sup>-1</sup>, which are within 20 cm<sup>-1</sup> of the experimental values 1594.7 cm<sup>-1</sup>, 3657.1 cm<sup>-1</sup> and 3755.9 cm<sup>-1</sup> [49, 50]. Note that the OH-stretch band consists of two modes, namely the low-frequency symmetric mode, where both OH bonds vibrate in phase, and the high-frequency anti-symmetric mode, where the OH bonds vibrate out of phase, which do not clearly separate in the liquid spectrum. The symmetric stretch mode in the gas phase shows a much smaller intensity than the anti-symmetric stretch mode, in agreement with experiment [50], which is caused by electronic polarization effects. The OH-stretch peak in the liquid is significantly red-shifted and enhanced compared to gas phase, which is typically rationalized by the softening of the OH bond potential and the constructive collectivity of OH-stretching vibrations in the liquid (see SI section II) [2, 3, 51]; the

significant enhancement is noteworthy, since one could expect the friction acting on the OH bond to be much stronger in the liquid and thus to reduce the vibrational amplitude. In contrast, the HOH-bending mode in the liquid is slightly blue-shifted and not enhanced, which can be rationalized by collective effects that are slightly destructive (see SI section II). All these effects are fully accounted for by the frequency-dependent friction acting on the different vibrational modes, as explained below.

The vibrational modes of a water molecule can be described by the bond angle  $\phi_{\text{HOH}}$  and the symmetric and anti-symmetric stretch distances,  $d_{\text{OHs}} = (d_{\text{OH1}} + d_{\text{OH2}})/2$  and  $d_{\text{OHa}} = (d_{\text{OH1}} - d_{\text{OH2}})/2$ , where the two OH bond distances in a water molecule are denoted as  $d_{\text{OH1}}$  and  $d_{\text{OH2}}$ , all based on the nuclear positions in the aiMD simulations, as illustrated in the inset in fig. 2C. The spectra of these three modes, averaged over all water molecules in the liquid, are shown in fig. 2C ( $\phi_{\text{HOH}}$  as dotted,  $d_{\text{OHs}}$  as solid and  $d_{\text{OHa}}$  as broken blue lines) and compared to the spectrum from the total dipole moment. The agreement of the line frequencies and shapes is quite good, except that the  $d_{\text{OHs}}$  and  $d_{\text{OHa}}$  spectra are blue-shifted compared to the polarization spectrum. This blue shift is due to the neglect of spectral correlations between neighboring water molecules as discussed above and the neglect of electronic degrees of freedom in the nuclear-position mode spectra, as shown in the SI section III. The  $d_{\text{OHs}}$  and  $d_{\text{OHa}}$  spectra overlap significantly, with a small red shift of the  $d_{\text{OHs}}$  spectrum relative to the  $d_{\text{OHa}}$  spectrum, in accordance with previous observations [52]. The spectrum of the  $\phi_{\text{HOH}}$  mode overlaps perfectly with the spectrum from the total (nuclear and electronic) dipole moment, which is due to the fact that the bending angle vibrations of neighboring water molecules are only weakly (and in fact anti-) correlated, as shown in the SI section II [51]. We conclude that the spectra calculated from the total system polarization (including nuclear and electronic polarization from all water molecules and their correlations) match the spectra based on the single-water nuclear-coordinate-based vibrational modes rather faithfully, which is at the heart of the common molecular interpretation of IR spectra and also validates our further approach.

In the following, we will analyze the dynamics of the water vibrational modes based on the one-dimensional GLE

$$m\ddot{x}(t) = - \int_0^t \Gamma(t-t')\dot{x}(t')dt' - \nabla U[x(t)] + F_R(t) \quad (1)$$

which contains a in general non-harmonic time-independent potential  $U(x)$  that corresponds to a free energy as it results from integrating out all other degrees of freedom except  $x(t)$ . The memory kernel  $\Gamma(t)$  describes the time-dependent friction acting on the fluctuating variable  $x(t)$ , which can be either the bond angle  $\phi_{\text{HOH}}$ , the symmetric or the anti-symmetric stretch distances,  $d_{\text{OHs}}$  or  $d_{\text{OHa}}$ . The random force  $F_R(t)$  has zero mean  $\langle F_R(t) \rangle = 0$  and fulfills the fluctuation-dissipation relation  $\langle F_R(t)F_R(t') \rangle = k_B T \Gamma(t-t')$ . Given a trajectory

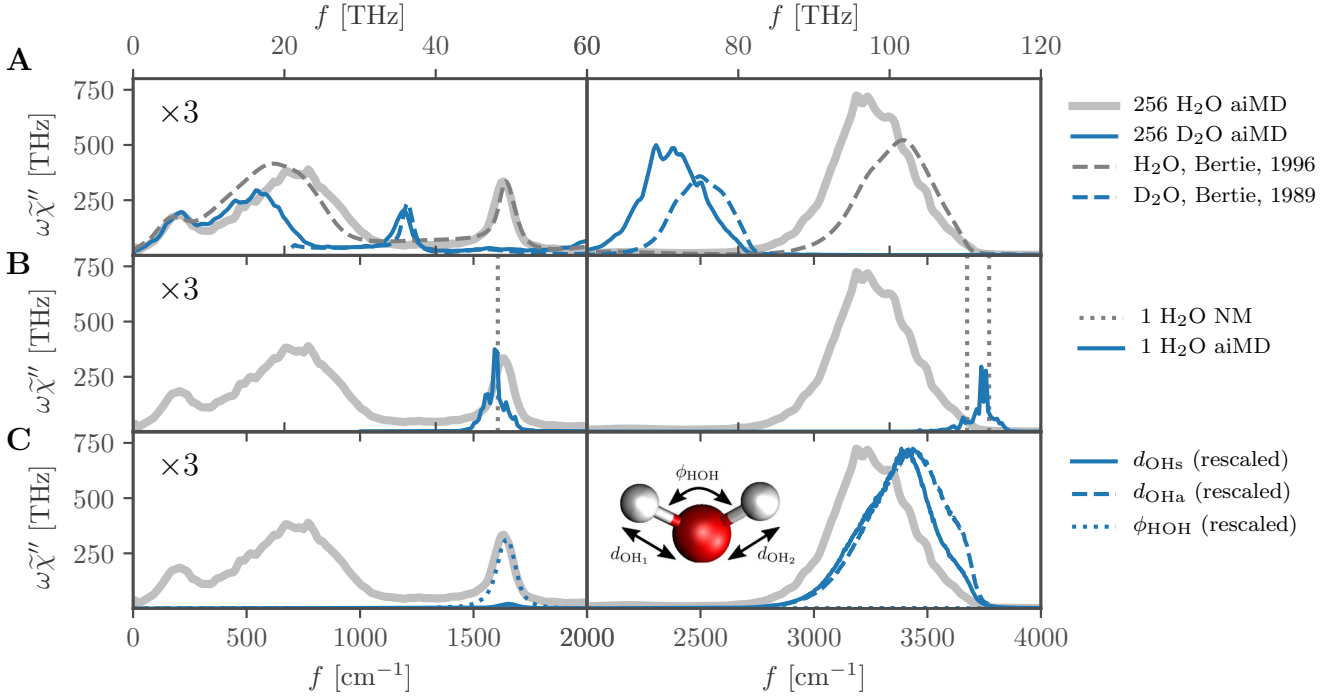


FIG. 2. Absorption spectra of aiMD simulations at 300 K of 256 H<sub>2</sub>O are shown as grey solid lines in A-C. The spectra up to 2000 cm<sup>-1</sup> are multiplied by a factor three. **A:** Comparison to aiMD spectra for liquid D<sub>2</sub>O (blue solid line) and experimental data (obtained for 298 K), shown as a grey broken line for H<sub>2</sub>O [42] and a blue broken line for D<sub>2</sub>O [43]. **B:** Comparison to aiMD simulations of a single H<sub>2</sub>O (blue solid line). The normal-mode frequencies of a single H<sub>2</sub>O are shown as vertical dotted lines. **C:** Comparison to power spectra of the symmetric stretch,  $d_{\text{OHs}}$  (blue solid line), anti-symmetric stretch,  $d_{\text{OHa}}$  (blue broken line), and bend modes,  $\phi_{\text{HOH}}$  (blue dotted line), that are averaged over all molecules and rescaled to match the absorption spectrum.

$x(t)$  from the aiMD simulations, the effective mass  $m$ , the potential  $U(x)$  and the friction function  $\Gamma(t)$  can be uniquely determined, as described in SI sections IV and V. As a crucial test of the validity of the GLE and of our extraction methods, we will further below demonstrate that the GLE accurately reproduces the mode spectra calculated directly from the aiMD simulations.

For a harmonic potential,  $U(x) = \frac{k}{2}x^2$ , the power spectrum can be given in closed form as (see SI section VI)

$$\omega\tilde{\chi}''(\omega) = \frac{\omega^2 \text{Re}\tilde{\Gamma}(\omega)}{|k - m\omega^2 - i\tilde{\Gamma}(\omega)\omega|^2} \quad (2)$$

where the frequency-dependent friction is obtained by a single-sided Fourier transform  $\tilde{\Gamma}(\omega) = \int_0^\infty dt e^{i\omega t}\Gamma(t)$ . In the limit of frequency-independent friction  $\tilde{\Gamma}(\omega) = \gamma$ , this yields the standard Lorentzian line shape [53] (see SI section VII)

$$\omega\tilde{\chi}''(\omega) = \frac{\omega^2\gamma}{(k - m\omega^2)^2 + \gamma^2\omega^2} \quad (3)$$

which will be shown to give only a poor account of our simulated spectra. Non-harmonic potentials are parametrized

as

$$U(x) = \frac{k}{2}(x - x_0)^2 + \frac{k_3}{3}(x - x_0)^3 + \frac{k_4}{4}(x - x_0)^4 \quad (4)$$

where  $x_0$  is the position of the minimum of  $U(x)$ . Spectra in the presence of non-harmonic potentials are obtained from numerical simulations of the GLE using a parametrized friction function of the form [54–56]

$$\Gamma(t) = \sum_{i=0}^n \frac{\gamma_i}{\tau_i^\epsilon} e^{-t/\tau_i^\epsilon} + \sum_{i=0}^l a_i e^{-t/\tau_i^\circ} \left[ \cos(\omega_i t) + \frac{1}{\tau_i^\circ \omega_i} \sin(\omega_i t) \right] \quad (5)$$

consisting of  $n$  exponentially decaying components with time scales  $\tau_i^\epsilon$  and friction coefficients  $\gamma_i$  as well as  $l$  oscillating and decaying components with amplitudes  $a_i$ , oscillation frequencies  $\omega_i$  and decay time scales  $\tau_i^\circ$ , see SI sections VIII–X for details.

### III. RESULTS AND DISCUSSION

We start with a discussion of the symmetric stretch mode  $d_{\text{OHs}}$ . The potential (or rather the free energy)

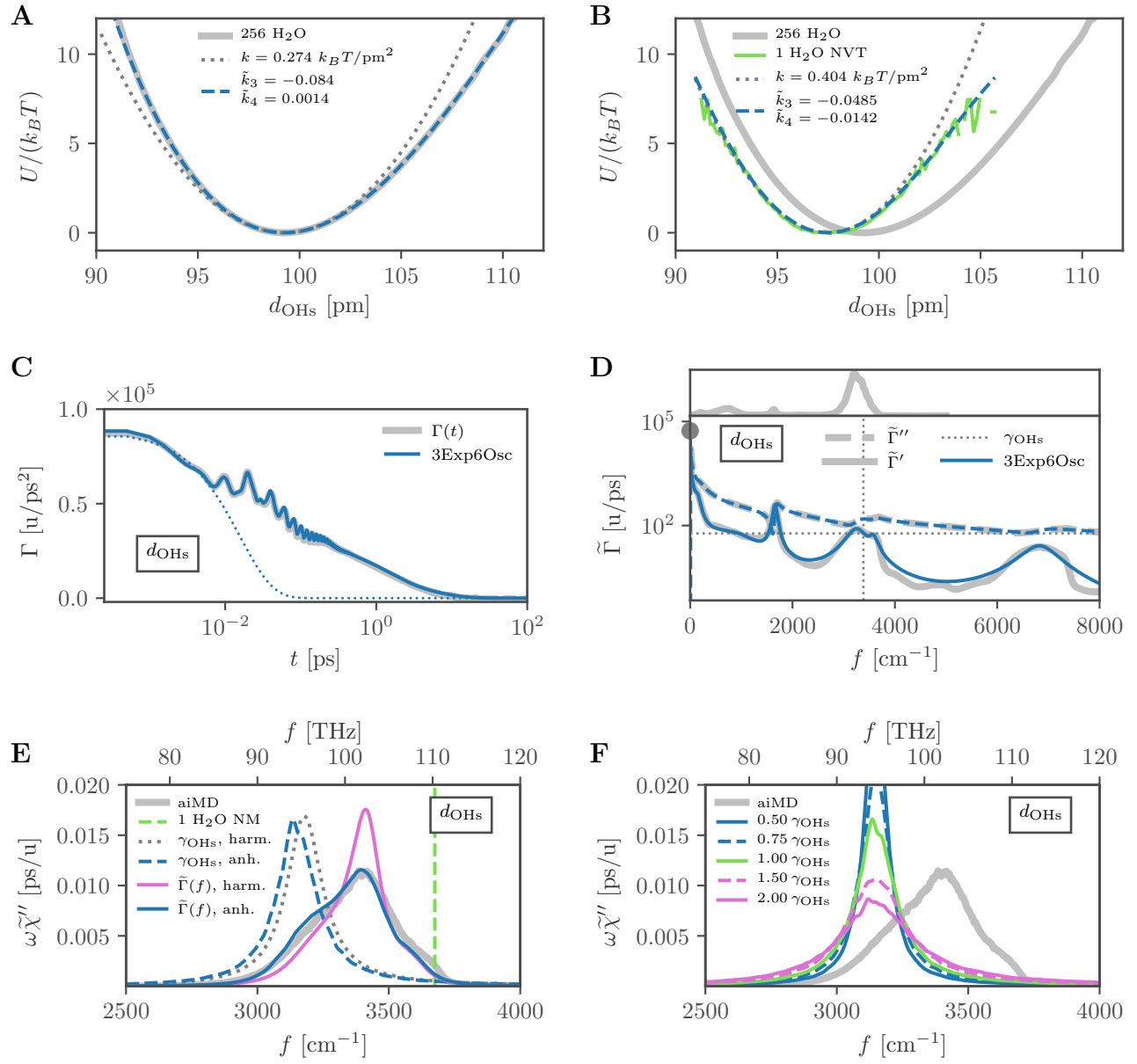


FIG. 3. Results for the symmetric stretch coordinate  $d_{\text{OHs}}$  from aiMD simulations. **A:** Potential  $U(d_{\text{OHs}})$  for 256 H<sub>2</sub>O in the liquid phase (grey solid line) compared to the non-harmonic fit according to eq. (4) (blue broken line) and the harmonic part (grey dotted line). **B:** Potential  $U(d_{\text{OHs}})$  for a single H<sub>2</sub>O (green solid line) compared with the non-harmonic fit according to eq. (4) (blue broken line) and the harmonic part (grey dotted line), the liquid-phase potential (grey solid line) is shown for comparison. **C, D:** Friction as a function of time and frequency (grey lines) compared with the fit according to eq. (5) (blue lines). Real and imaginary parts in (D) are shown as solid and broken lines, the spectrum on top is the full absorption spectrum from aiMD. The blue dotted line in (C) shows a single exponential with decay time  $\tau = 10$  fs, the dotted horizontal line in (D) shows the constant real friction  $\gamma_{\text{OHs}} = \tilde{\Gamma}'(f_{\text{OHs}})$  evaluated at the symmetric OH stretch vibrational frequency  $f_{\text{OHs}} = 3390 \text{ cm}^{-1}$ . The grey circle denotes the static friction  $\tilde{\Gamma}(0)$ . **E:** Power spectrum  $\omega \tilde{\chi}''$  (grey solid line) compared to models of varying complexity: normal mode of single H<sub>2</sub>O (broken vertical line), Lorentzian with harmonic potential and constant friction  $\gamma_{\text{OHs}}$  (grey dotted line), non-harmonic potential and constant friction  $\gamma_{\text{OHs}}$  (blue broken line), harmonic potential and frequency-dependent friction  $\tilde{\Gamma}(f)$  (purple solid line), non-harmonic potential and frequency-dependent friction  $\tilde{\Gamma}(f)$  (blue solid line). **F:** Power spectrum  $\omega \tilde{\chi}''$  using the non-harmonic potential and different values of the constant friction  $\gamma$ , where  $\gamma_{\text{OHs}} = \tilde{\Gamma}'(f_{\text{OHs}})$  is the friction evaluated at the symmetric OH stretch vibrational frequency.

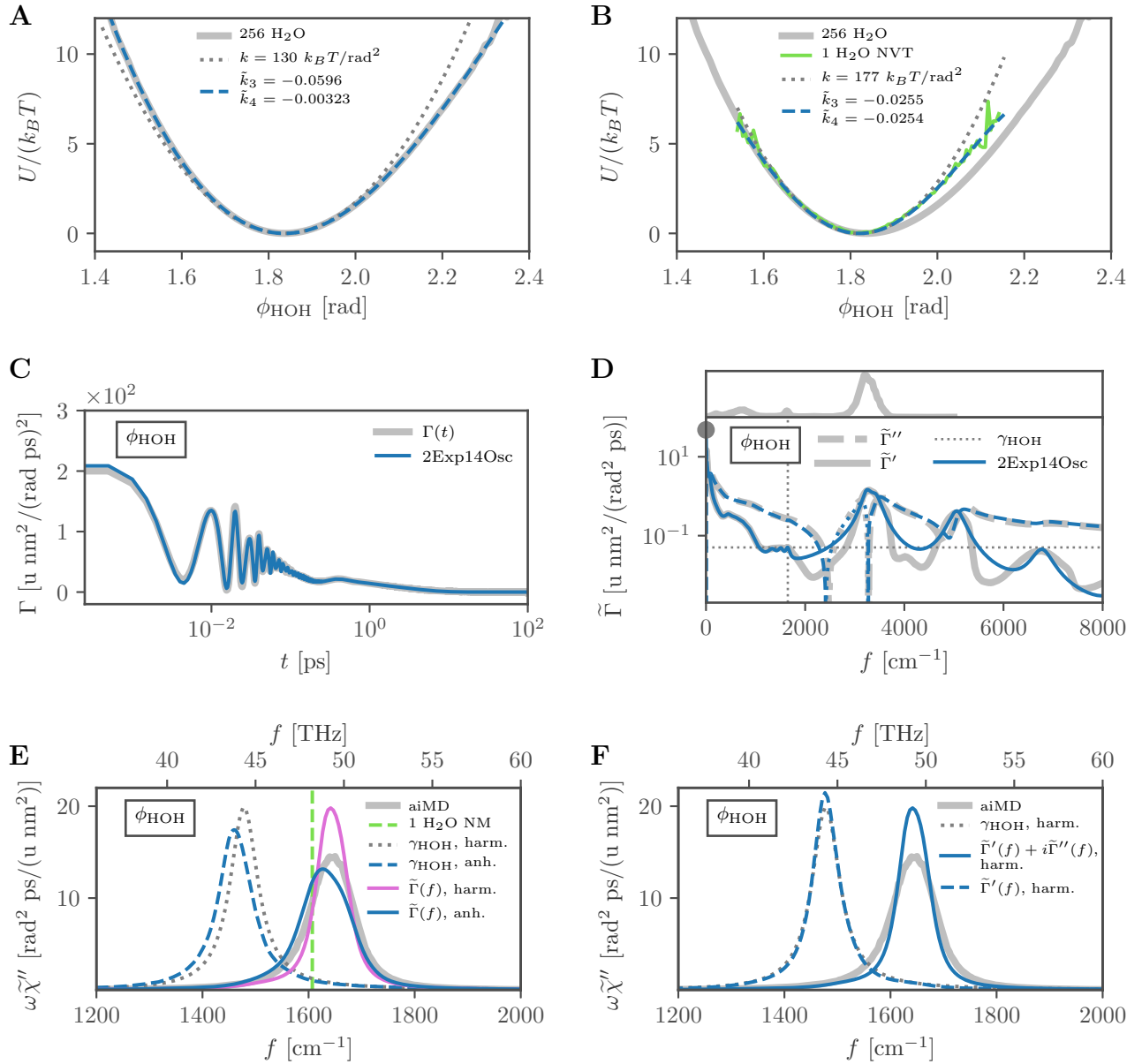


FIG. 4. Results for the bend coordinate  $\phi_{\text{HOH}}$  from aiMD simulations. **A**: Potential  $U(\phi_{\text{HOH}})$  for 256 H<sub>2</sub>O in the liquid phase (grey solid line) compared to the non-harmonic fit according to eq. (4) (blue broken line) and the harmonic part (grey dotted line). **B**: Potential  $U(\phi_{\text{HOH}})$  for a single H<sub>2</sub>O (green solid line) compared with the non-harmonic fit according to eq. (4) (blue broken line) and the harmonic part (grey dotted line), the liquid-phase potential (grey solid line) is shown for comparison. **C**, **D**: Friction as a function of time and frequency (grey lines) compared with the fit according to eq. (5) (blue lines). Real and imaginary parts in (D) are shown as solid and broken lines, dotted lines denote negative values of the imaginary part, the spectrum on top is the full absorption spectrum from aiMD. The dotted horizontal line in (D) shows the constant real friction  $\gamma_{\text{HOH}} = \tilde{\Gamma}'(f_{\text{HOH}})$  evaluated at the bend vibrational frequency  $f_{\text{HOH}} = 1650 \text{ cm}^{-1}$ . The grey circle denotes the static friction  $\tilde{\Gamma}'(0)$ . **E**: Power spectrum  $\omega\tilde{\chi}''$  (grey solid line) compared to different models: normal mode of single H<sub>2</sub>O (broken vertical line), Lorentzian with harmonic potential and constant friction  $\gamma_{\text{HOH}}$  (grey dotted line), non-harmonic potential and constant friction  $\gamma_{\text{HOH}}$  (blue broken line), harmonic potential and frequency-dependent friction  $\tilde{\Gamma}(f)$  (purple solid line), non-harmonic potential and frequency-dependent friction  $\tilde{\Gamma}(f)$  (blue solid line). **F**: Power spectrum  $\omega\tilde{\chi}''$  using the harmonic potential part and the constant friction  $\gamma_{\text{HOH}}$  (grey broken line), the real frequency-dependent friction only  $\tilde{\Gamma}'(f)$  (blue broken line), the real and imaginary frequency-dependent friction  $\tilde{\Gamma}'(f) + i\tilde{\Gamma}''(f)$  (blue solid line). The grey solid line is the spectrum from aiMD simulations.

$U(d_{\text{OHs}})$  from the aiMD simulations for liquid water (grey solid line) is in fig. 3A compared with a non-harmonic fit according to eq. (4) (blue broken line), the harmonic contribution is shown as a grey dotted line. The comparison of the liquid and gas-phase bond potentials in fig. 3B shows that the minimum of the potential (i.e. the most probable OH bond length) increases from  $x_0 = 97.50$  pm in the gas phase to  $x_0 = 99.25$  pm in the liquid; at the same time the harmonic force constant decreases from  $k/k_B T = 0.404$  pm $^{-2}$  in the gas phase to  $k/k_B T = 0.274$  pm $^{-2}$  in the liquid. This softening of the potential is due to elongation of the bond, caused by hydrogen bonding in the liquid, and will be shown to induce a pronounced spectral red shift. Furthermore, the potential non-harmonicity increases, as can be seen by comparing the reduced cubic potential coefficient in the liquid phase  $\tilde{k}_3 = k_3/k_B T (k/k_B T)^{-3/2} = -0.0840$  with the value in the gas phase  $\tilde{k}_3 = -0.0485$ .

The time-dependent friction function for the symmetric stretch mode  $\Gamma(t)$  extracted from aiMD simulations, grey line in fig. 3C, shows multi-exponential decay characterized by relaxation times from a few fs to many ps, which is appreciated by comparison with a single-exponential function with decay time  $\tau = 10$  fs (dotted blue line, the logarithmic time axis should be noted). This in particular means that  $\Gamma(t)$  accounts for solvent relaxations that are fast (adiabatic) and slow (non-adiabatic) with respect to the OH vibrational period of 10 fs; one thus expects homogeneous as well as inhomogeneous line broadening to occur, as indeed borne out by our analysis below. The oscillations that appear in  $\Gamma(t)$  at around 10 fs to 250 fs reflect the dissipative coupling of symmetric stretch vibrations to anti-symmetric stretch as well as higher-harmonic bend and librational modes. This is illustrated by the real and imaginary frequency-dependent friction components  $\tilde{\Gamma}'(\omega) + i\tilde{\Gamma}''(\omega) = \int_0^\infty dt e^{i\omega t} \Gamma(t)$  in fig. 3D (solid and broken grey lines, respectively), which exhibit maxima at the OH-stretching and HOH-bending frequencies and also at their higher harmonics. The friction function thus details the vibrational energy dissipation of a given vibrational mode within a water molecule as well as with the surrounding water and in particular accounts for Fermi resonances between different vibrational modes (albeit on the classical level). Also non-Condon effects, which arise due to modifications of the transition dipole moment of a vibrational mode due to time-dependent changes of the solvation environment of a molecule [35], are included via the interplay of the potential  $U(d_{\text{OHs}})$  and the time-dependent friction function  $\Gamma(t)$ . Interestingly, the symmetric stretch shows a much stronger frictional damping at the characteristic frequency of the bending mode than the anti-symmetric stretch mode, shown in SI section XI, which points to a stronger dissipative coupling of bending vibrations with symmetric than with anti-symmetric stretch vibrations. For simulations of the GLE, which are necessary for the analysis of the coupling between non-linearities in the potential and frequency-dependent friction, we fit  $\tilde{\Gamma}'(\omega)$  by the expression eq. (5) with a sum

of three exponential and six oscillating functions, see SI section VIII for details. The fit shown in blue in figs. 3C and D describes the simulated friction function equally well in the time as well as in the frequency domain.

The vibrational spectrum of the  $d_{\text{OHs}}$  mode directly extracted from aiMD simulations is shown in fig. 3E as a grey solid line. The simplest possible model for a vibrational line shape is the Lorentzian model eq. (3) for a harmonic potential and a constant, frequency-independent friction. Using  $k/k_B T = 0.274$  pm $^{-2}$  from the harmonic fit in fig. 3A and the friction  $\gamma_{\text{OHs}} = \tilde{\Gamma}'(f_{\text{OHs}})$  in fig. 3D at the stretch vibrational frequency  $f_{\text{OHs}} = 3390$  cm $^{-1}$ , we obtain the grey dotted line in fig. 3E. Compared to the normal-mode frequency of the gas phase, denoted by a vertical green broken line, the Lorentzian is significantly red-shifted by about 500 cm $^{-1}$ , the width of the Lorentzian reflects homogeneous line broadening due to adiabatic solvent friction that is described by the frequency-independent constant  $\gamma_{\text{OHs}}$ . Note that the Lorentzian is considerably red-shifted and narrower compared to the spectrum extracted from the aiMD simulation (grey line). Interestingly, the friction  $\gamma_{\text{OHs}}$  that acts at the vibration frequency  $f_{\text{OHs}}$  is about two orders of magnitude smaller than the friction in the static limit  $f = 0$ , as seen in fig. 3D, which explains why the stretch vibrational dynamics shown in fig. 1A is rather weakly damped. The power spectrum in the presence of the full non-harmonic potential  $U(d_{\text{OHs}})$  and constant friction  $\gamma_{\text{OHs}}$ , obtained from numerical simulations of the regular Langevin equation (blue broken line, see SI section IX for details), is only slightly red-shifted with respect to the Lorentzian obtained for a harmonic potential, which is expected based on perturbation theory [4]. We conclude that non-linearities in the potential have for constant friction only an insignificant influence on the line frequency and shape. The peak frequency of a Lorentzian does not depend on the value of the constant friction  $\gamma$  (see SI section XII), which is approximately true also in the presence of the non-harmonic potential  $U(d_{\text{OHs}})$ , as demonstrated in fig. 3F where spectra from numerical simulations for varying  $\gamma$  are compared. We next check for the influence of time-dependent friction on the spectrum. For a harmonic potential and for frequency-dependent friction, the spectrum is determined analytically by eq. (2) and shown in fig. 3E as a purple solid line. A significant blue shift compared to the results for constant friction is obtained, so that the position of the spectrum agrees very well with the simulated spectrum, while the line shape is too narrow. The blue shift can be understood based on simple and rather general analytic arguments, as shown below. The spectrum obtained from the GLE in the presence of the non-harmonic potential  $U(d_{\text{OHs}})$  and time-dependent friction  $\Gamma(t)$ , shown by the blue solid line in fig. 3E (here numerical simulations are employed), is significantly broadened compared to the results obtained for a harmonic potential and time-dependent friction  $\Gamma(t)$  (purple line). This reflects the effects of inhomogeneous line broadening [4], and reproduces the spectrum extracted

from the aiMD simulations (grey line) almost perfectly; in fact, inhomogeneous line broadening is quite substantial and accounts for 52% of the total line broadening. This means that the GLE, when used in conjunction with the properly extracted non-harmonic time-averaged potential  $U(d_{\text{OHs}})$  and time-dependent friction  $\Gamma(t)$ , reproduces the system dynamics very well, which is not guaranteed in general since the projection onto the GLE neglects non-linear friction effects [30].

The  $\phi_{\text{HOH}}$  water bending coordinate is analyzed analogously: The bend angle potential  $U(\phi_{\text{HOH}})$  in fig. 4A extracted from aiMD simulations (grey line) includes significant non-linear contributions as appreciated by a comparison of the non-harmonic fit (blue broken line) with the harmonic part (dotted line) and as witnessed by the magnitude of the reduced cubic and quartic fit parameters  $\tilde{k}_3 = -0.0596$  and  $\tilde{k}_4 = k_4/k_B T (k/k_B T)^{-2} = -0.00323$ . Different from the situation for the stretch potential, the liquid environment shifts the most probable bending angle only very slightly. The potential is softened considerably, as is seen by a comparison of the shape and fit parameters of the gas and liquid phase potentials  $U(\phi_{\text{HOH}})$  in fig. 4B, which can be rationalized by the fact that attractive electrostatic interactions, which are predominant for strongly correlated polar liquids such as water, exhibit negative curvature throughout their entire interaction range. The time-dependent friction  $\Gamma(t)$  extracted from the simulations in fig. 4C (grey line) shows a broad decay but more pronounced oscillations compared to the stretch vibrations in fig. 3C. The fit (blue solid line) to the simulated real frequency-dependent friction  $\tilde{\Gamma}'(f)$  (grey solid line) in fig. 4D requires two exponential and 14 oscillatory functions to describe the simulated data satisfactorily, see SI section VIII for details. The dissipative damping is significantly more pronounced at stretch frequencies around  $3400 \text{ cm}^{-1}$  and at the overtones of the bending around  $3300 \text{ cm}^{-1}$  and around  $4950 \text{ cm}^{-1}$  than at the bending fundamental around  $1650 \text{ cm}^{-1}$  itself, indicative of the non-linear coupling between different modes and overtones (where it should be noted that coupling of bend vibrations to higher-frequency modes and overtones are reduced when quantum effects are properly included [15]).

The vibrational spectrum of the  $\phi_{\text{HOH}}$  coordinate from the aiMD simulations is shown in fig. 4E as a grey solid line and is weakly blue-shifted from the gas phase normal mode (vertical green broken line), which is a surprising fact and will be explained now by compensatory potential and friction effects. The spectrum from the Lorentzian model eq. (3) (grey dotted line) using only the harmonic potential part of  $U(\phi_{\text{HOH}})$  and the frequency-independent friction  $\gamma_{\text{HOH}} = \tilde{\Gamma}'(f_{\text{HOH}})$ , obtained at the bending peak at  $f_{\text{HOH}} = 1650 \text{ cm}^{-1}$  (horizontal broken line in fig. 4D), is significantly red-shifted and is not modified much by including the non-harmonic potential contributions (blue broken line). Including the complex frequency-dependent friction  $\tilde{\Gamma}(f)$  but only the harmonic part of  $U(\phi_{\text{HOH}})$  the purple line is obtained, which is blue shifted with respect to the constant-friction case and reaches the frequency

of the simulated curve but is too narrow. Including the complex frequency-dependent friction  $\tilde{\Gamma}(f)$  and also the full non-harmonic potential  $U(\phi_{\text{HOH}})$ , the GLE (indicated by the blue line) rather accurately reproduces the position and width of the simulated spectrum. In agreement with our stretch-vibration results in fig. 3E, we detect considerable inhomogeneous line broadening (amounting to 47% of the total line broadening) from the comparison of the results with and without non-harmonic potential contributions in the presence of frequency-dependent friction. In contrast to the stretch-vibration results, we see that the blue shift induced by including the frequency dependence of the friction almost exactly cancels the red shift due to the softening of the bond potential in the liquid phase, which means that the frequency dependence of  $\tilde{\Gamma}(f)$  close to the characteristic bend-mode frequency is more pronounced compared to the stretch mode.

It turns out that the imaginary and real parts of the frequency-dependent friction influence the line position and shape quite differently [25]. This is illustrated in fig. 4F by comparing spectra using only the harmonic part of the potential for constant friction (grey dotted line), for purely real frequency-dependent friction  $\tilde{\Gamma}'(f)$  (blue broken line) and for friction that contains both real and imaginary frequency-dependent parts  $\tilde{\Gamma}'(f) + i\tilde{\Gamma}''(f)$  (blue solid line), note that for purely imaginary friction the spectrum according to eq. (2) exhibits a singularity and thus is not shown. It is in fact the imaginary part  $\tilde{\Gamma}''(f)$  that gives rise to the blue shift, as is now explained by a simple analytical argument.

For this we consider a single-exponential memory function  $\Gamma(t) = \gamma\tau^{-1} \exp(-t/\tau)$ . The single-sided Fourier transform is given as  $\tilde{\Gamma}(\omega) = \int_0^\infty dt e^{i\omega t} \Gamma(t) = \gamma/(1 - i\tau\omega)$  with the asymptotic limits  $\tilde{\Gamma}(\omega) \simeq \gamma(1 + i\omega\tau)$  for small  $\omega$  and  $\tilde{\Gamma}(\omega) \simeq i\gamma/(\omega\tau)$  for large  $\omega$ , both deviations from the zero-frequency limit  $\tilde{\Gamma}(\omega \rightarrow 0) \simeq \gamma$  turn out to be imaginary, which already hints at why the imaginary part of the friction determines the line position, as demonstrated in fig. 4F. A general form that contains both asymptotic limits is given by  $\tilde{\Gamma}(\omega) \simeq \gamma + ia\omega + ib/\omega$ , where  $a = \gamma\tau$  and  $b = 0$  for small  $\omega$  and  $a = 0$  and  $b = \gamma/\tau$  for large  $\omega$ . By inserting this asymptotic form into eq. (2), the Lorentzian line shape eq. (3) is recovered but with an effective mass  $m_{\text{eff}} = m - a$  and an effective potential curvature  $k_{\text{eff}} = k + b$ . The vibrational frequency turns out to be

$$\omega_0 = \sqrt{\frac{k_{\text{eff}}}{m_{\text{eff}}}} = \sqrt{\frac{k + b}{m - a}} \quad (6)$$

and in fact increases both in the small and large frequency limits, since  $a$  and  $b$  are positive constants for single-exponential memory. Thus, a blue shift of the vibrational frequency is very generally expected for frequencies where the frequency-dependent friction is described by the asymptotic form  $\tilde{\Gamma}(\omega) \simeq \gamma + ia\omega + ib/\omega$  with positive  $a$  and  $b$ . In fact, this functional form is able to describe the stretch and band friction functions rather accurately



around the stretch and band frequencies, respectively, as inspection of figs. 3D and 4D shows.

The full width at half maximum of a Lorentzian is given as  $\gamma/m_{\text{eff}} \simeq \gamma/(m - a)$ ; thus the line width is, within the harmonic approximation, predicted to slightly increase for the stretch band (since  $\tilde{\Gamma}''(f)$  slightly increases at the stretch vibrational frequency in fig. 3D and thus  $a$  is positive) but to stay rather constant for the bend band (since  $\tilde{\Gamma}''(f)$  slightly decreases at the stretch vibrational frequency fig. 4D and thus  $a$  presumably is small and dominated by  $b$ ). These predictions are in good agreement with the results shown in figs. 3E and 4E for the scenario of a harmonic potential and friction-dependent friction (purple lines). Clearly, the exact line shape and position are determined by the interplay of non-linearities of the potential and frequency-dependent friction, but the simple harmonic model discussed here allows to appreciate part of the mechanisms at play.

#### IV. CONCLUSIONS

While frequency-independent friction, which reflects the fast adiabatic dissipative channels available for a specific vibration, mostly modifies the line width via homogeneous line broadening, but not the line position, which holds approximately even in the presence of non-linear potential contributions, the full frequency dependence of the friction, which in particular accounts for the slower solvent relaxation processes, gives rise to a blue shift and additional line broadening, the latter reflects what is typically called inhomogeneous line broadening. In contrast, softening of the bond potential in the liquid environment, which is due to hydrogen bonding and hydration interactions, gives rise to a red shift. So we find that the line shapes and positions of the bend and stretch bands in liquid water can be understood by a careful discussion of the compensatory effects of frequency-dependent friction and harmonic as well as non-harmonic potential contributions. For stretch vibrations, the bond softening dominates and therefore the stretch vibration is red-shifted when going from gas to liquid water; for bend vibrations the potential-induced red shift and the friction-induced blue shift almost exactly compensate. This of course does not imply that the coupling of bend vibrations to the hydrating liquid environment is weaker than for stretch vibrations, as one might naively guess from only looking at the frequency shifts, rather the contrary is true. It turns out that it is the imaginary part of the frequency-dependent friction that gives rise to the blue shift, in line with previous arguments [25]. The situation is rather complex, though, since the effects due to the frequency-dependency of the friction and due to non-linearities in the potential do not decouple. Our methodology is different from previous approaches to describe the infrared line shapes of water [6, 57], since we deploy the time-averaged bond potential as it is defined in the GLE. This in particular means that in our approach, inhomogeneous line broadening en-

ters via the time-dependent friction function, not via a time-dependent bond potential.

As mentioned before, our *ab initio* simulations neglect nuclear quantum effects [47, 48], owing to the fact that methods to extract friction functions from path-integral simulations are not yet available. This approximation presumably is permissible in the present context, as we target the general compensatory effects the liquid environment has on bond potentials and the bond friction function, which should not be fundamentally changed by nuclear quantum effects. In the future, it would be interesting to extract GLE parameters from path integral simulations [47, 48] and from mixed quantum/classical approaches [31, 33, 58].

#### V. METHODS

All Born-Oppenheimer aiMD simulations were performed with the CP2K 4.1 software package using a double- $\zeta$  basis set for the valence electrons, optimized for small molecules and short ranges, (DZVP-MOLOPT-SR-GTH), dual-space pseudopotentials, the BLYP exchange-correlation functional, D3 dispersion correction and a cutoff for the plane-wave representation set to 400 Ry [59–61]. The aiMD simulations were performed using a time step of 0.5 fs under NVT conditions at 300 K by coupling all atoms to a CSV thermostat with a time constant of 100 fs [62]. The bulk systems contain 256 molecules subject to periodic boundary conditions in a cubic cell of size  $(1.9734 \text{ nm})^3$ , corresponding to densities of  $996.4 \text{ kg/m}^3$  for  $\text{H}_2\text{O}$  and  $1107.8 \text{ kg/m}^3$  for  $\text{D}_2\text{O}$ . The total trajectory lengths of the liquid systems are 230 ps for  $\text{H}_2\text{O}$  and 130 ps for  $\text{D}_2\text{O}$ . Simulations of single  $\text{H}_2\text{O}$ , representing the gas phase data, were performed in the NVE ensemble with 47 initial configurations sampled from a 25 ps NVT simulation using an individual thermostat with a time constant of 10 fs for each atom. The NVE simulations were each run for 10 ps with a time step of 0.25 fs. The distributions of their initial configurations sample well the equilibrium distributions as shown in SI section XIII.

Linear response theory relates the dielectric susceptibility  $\chi(t)$  to the equilibrium autocorrelation of the dipole moment  $C(t) = \langle \mathbf{p}(t)\mathbf{p}(0) \rangle$ , reading in Fourier space [63]

$$\tilde{\chi}(\omega) = \frac{1}{V\epsilon_0 k_B T} \left( C(0) - i\frac{\omega}{2}\tilde{C}^+(\omega) \right) \quad (7)$$

with system volume  $V$ , thermal energy  $k_B T$  and vacuum permittivity  $\epsilon_0$ . IR spectra can therefore be calculated straight-forwardly from sufficiently long trajectories from aiMD simulation data using eq. (7) and the Wiener-Kintchine relation [51, 64], derived in SI section XIV. Quantum corrections have previously been addressed, but were not applied here [65]. The molecular dipole moments are obtained after Wannier-center localization of the electron density at a time resolution of 2 fs. The Wannier

centers were assigned to the molecule of the nearest oxygen, which always results in exactly four Wannier centers per water molecule. A charge of  $-2e$  is assigned to each Wannier center, which together with the nuclear charges, reduced by the electronic charges of the inner shells, allows for the calculation of the dipole moment. The power spectra are smoothed using a Gaussian kernel with width  $10\text{ cm}^{-1}$ . The normal mode analysis was performed for an energetically minimal configuration of a single  $\text{H}_2\text{O}$  using the implementation in CP2K 4.1 and the same ab initio model as for the aiMD simulation.

## ACKNOWLEDGMENTS

We gratefully acknowledge support by the DFG grants SFB 1078 and SFB 1114, the MaxWater initiative from the Max Planck Society, the ERC Advanced Grant grant agreement No. [835117], computing time on the HPC cluster at ZEDAT, FU Berlin and the computational resources provided by the North-German Supercomputing Alliance (HLRN) under project bep00068.

- 
- [1] Falk, M. The frequency of the HOH bending fundamental in solids and liquids. *Spectrochim. Acta Part A Mol. Spectrosc.* **1984**, *40*, 43–48.
- [2] Bakker, H. J.; Skinner, J. L. Vibrational spectroscopy as a probe of structure and dynamics in liquid water. *Chem. Rev.* **2010**, *110*, 1498–1517.
- [3] Perakis, F.; Marco, L. D.; Shalit, A.; Tang, F.; Kann, Z. R.; Kühne, T. D.; Torre, R.; Bonn, M.; Nagata, Y. Vibrational Spectroscopy and Dynamics of Water. *Chem. Rev.* **2016**, *116*, 7590–7607.
- [4] Oxtoby, D. W.; Levesque, D.; Weis, J. J. A molecular dynamics simulation of dephasing in liquid nitrogen. *J. Chem. Phys.* **1978**, *68*, 5528–5533.
- [5] Møller, K. B.; Rey, R.; Hynes, J. T. Hydrogen bond dynamics in water and ultrafast infrared spectroscopy: A theoretical study. *J. Phys. Chem. A* **2004**, *108*, 1275–1289.
- [6] Auer, B. M.; Skinner, J. L. IR and Raman spectra of liquid water: Theory and interpretation. *J. Chem. Phys.* **2008**, *128*, 224511.
- [7] Lock, A. J.; Bakker, H. J. Temperature dependence of vibrational relaxation in liquid  $\text{H}_2\text{O}$ . *J. Chem. Phys.* **2002**, *117*, 1708–1713.
- [8] Cowan, M. L.; Bruner, B. D.; Huse, N.; Dwyer, J. R.; Chugh, B.; Nibbering, E. T.; Elsaesser, T.; Miller, R. J. Ultrafast memory loss and energy redistribution in the hydrogen bond network of liquid  $\text{H}_2\text{O}$ . *Nature* **2005**, *434*, 199–202.
- [9] Badger, R. M. A relation between internuclear distances and bond force constants. *J. Chem. Phys.* **1934**, *2*, 128–131.
- [10] Mikenda, W. Stretching frequency versus bond distance correlation of  $\text{O}-\text{D}(\text{H}) \cdots \text{Y}$  ( $\text{Y} = \text{N}, \text{O}, \text{S}, \text{Se}, \text{Cl}, \text{Br}, \text{I}$ ) hydrogen bonds in solid hydrates. *J. Mol. Struct.* **1986**, *147*, 1–15.
- [11] Boyer, M. A.; Marsalek, O.; Heindel, J. P.; Markland, T. E.; McCoy, A. B.; Xantheas, S. S. Beyond Badger’s Rule: The Origins and Generality of the Structure-Spectra Relationship of Aqueous Hydrogen Bonds. *J. Phys. Chem. Lett.* **2019**, *10*, 918–924.
- [12] Ashihara, S.; Huse, N.; Espagne, A.; Nibbering, E. T.; Elsaesser, T. Vibrational couplings and ultrafast relaxation of the O-H bending mode in liquid  $\text{H}_2\text{O}$ . *Chem. Phys. Lett.* **2006**, *424*, 66–70.
- [13] Van Der Post, S. T.; Hsieh, C.-S. S.; Okuno, M.; Nagata, Y.; Bakker, H. J.; Bonn, M.; Hunger, J. Strong frequency dependence of vibrational relaxation in bulk and surface water reveals sub-picosecond structural heterogeneity. *Nat. Commun.* **2015**, *6*, 8384.
- [14] Ashihara, S.; Huse, N.; Espagne, A.; Nibbering, E. T.; Elsaesser, T. Ultrafast structural dynamics of water induced by dissipation of vibrational energy. *J. Phys. Chem. A* **2007**, *111*, 743–746.
- [15] Rey, R.; Ingrosso, F.; Elsaesser, T.; Hynes, J. T. Pathways for  $\text{H}_2\text{O}$  bend vibrational relaxation in liquid water. *J. Phys. Chem. A* **2009**, *113*, 8949–8962.
- [16] Yu, C.-C. C.; Chiang, K.-Y. Y.; Okuno, M.; Seki, T.; Ohto, T.; Yu, X.; Korepanov, V.; Hamaguchi, H.-o. o.; Bonn, M.; Hunger, J.; Nagata, Y. Vibrational couplings and energy transfer pathways of water’s bending mode. *Nat. Commun.* **2020**, *11*, 5977.
- [17] Ma, A.; Stratt, R. M. Multiphonon vibrational relaxation in liquids: Should it lead to an exponential-gap law? *J. Chem. Phys.* **2004**, *121*, 11217–11226.
- [18] Lange, O. F.; Grubmüller, H. Collective Langevin dynamics of conformational motions in proteins. *J. Chem. Phys.* **2006**, *124*, 214903.
- [19] Horenko, I.; Hartmann, C.; Schütte, C.; Noe, F. Data-based parameter estimation of generalized multidimensional Langevin processes. *Phys. Rev. E* **2007**, *76*, 1–9.
- [20] Darve, E.; Solomon, J.; Kia, A. Computing generalized Langevin equations and generalized Fokker-Planck equations. *Proc. Natl. Acad. Sci.* **2009**, *106*, 10884–10889.
- [21] Lesnicki, D.; Vuilleumier, R.; Carof, A.; Rotenberg, B. Molecular Hydrodynamics from Memory Kernels. *Phys. Rev. Lett.* **2016**, *116*, 147804.
- [22] Deichmann, G.; Van der Vegt, N. F. Bottom-up approach to represent dynamic properties in coarse-grained molecular simulations. *J. Chem. Phys.* **2018**, *149*, 244114.
- [23] Jung, G.; Hanke, M.; Schmid, F. Generalized Langevin dynamics: construction and numerical integration of non-Markovian particle-based models. *Soft Matter* **2018**, *14*, 9368–9382.
- [24] Meyer, H.; Voigtmann, T.; Schilling, T. On the dynamics of reaction coordinates in classical, time-dependent, many-body processes. *J. Chem. Phys.* **2019**, *150*, 174118.
- [25] Metiu, H.; Oxtoby, D. W.; Freed, K. F. Hydrodynamic theory for vibrational relaxation in liquids. *Phys. Rev. A* **1977**, *15*, 361–371.
- [26] Whitnell, R. M.; Wilson, K. R.; Hynes, J. T. Vibrational relaxation of a dipolar molecule in water. *J. Chem. Phys.* **1992**, *96*, 5354–5369.
- [27] Tuckerman, M.; Berne, B. J. Vibrational relaxation in simple fluids: Comparison of theory and simulation. *J. Chem. Phys.* **1993**, *98*, 7301–7318.
- [28] Gnanakaran, S.; Hochstrasser, R. M. Vibrational relax-

- ation of HgI in ethanol: Equilibrium molecular dynamics simulations. *J. Chem. Phys.* **1996**, *105*, 3486–3496.
- [29] Joutsuka, T.; Ando, K. Vibrational spectroscopy and relaxation of an anharmonic oscillator coupled to harmonic bath. *J. Chem. Phys.* **2011**, *134*, 204511.
- [30] Gottwald, F.; Ivanov, S. D.; Kühn, O. Applicability of the Caldeira-Leggett model to vibrational spectroscopy in solution. *J. Phys. Chem. Lett.* **2015**, *6*, 2722–2727.
- [31] Lawrence, C. P.; Skinner, J. L. Vibrational spectroscopy of HOD in liquid D<sub>2</sub>O. VI. Intramolecular and intermolecular vibrational energy flow. *J. Chem. Phys.* **2003**, *119*, 1623–1633.
- [32] Ramasesha, K.; De Marco, L.; Mandal, A.; Tokmakoff, A. Water vibrations have strongly mixed intra- and intermolecular character. *Nat. Chem.* **2013**, *5*, 935–940.
- [33] Kananenka, A. A.; Skinner, J. L. Fermi resonance in OH-stretch vibrational spectroscopy of liquid water and the water hexamer. *J. Chem. Phys.* **2018**, *148*, 244107.
- [34] Matt, S. M.; Ben-Amotz, D. Influence of Intermolecular Coupling on the Vibrational Spectrum of Water. *J. Phys. Chem. B* **2018**, *122*, 5375–5380.
- [35] Schmidt, J. R.; Corcelli, S. A.; Skinner, J. L. Pronounced non-Condon effects in the ultrafast infrared spectroscopy of water. *J. Chem. Phys.* **2005**, *123*, 044513.
- [36] De Marco, L.; Carpenter, W.; Liu, H.; Biswas, R.; Bowman, J. M.; Tokmakoff, A. Differences in the Vibrational Dynamics of H<sub>2</sub>O and D<sub>2</sub>O: Observation of Symmetric and Antisymmetric Stretching Vibrations in Heavy Water. *J. Phys. Chem. Lett.* **2016**, *7*, 1769–1774.
- [37] Carpenter, W. B.; Fournier, J. A.; Biswas, R.; Voth, G. A.; Tokmakoff, A. Delocalization and stretch-bend mixing of the HOH bend in liquid water. *J. Chem. Phys.* **2017**, *147*, 084503.
- [38] Ojha, D.; Karhan, K.; Kühne, T. D. On the Hydrogen Bond Strength and Vibrational Spectroscopy of Liquid Water. *Sci. Rep.* **2018**, *8*, 16888.
- [39] Daldrop, J. O.; Kappler, J.; Brüning, F. N.; Netz, R. R. Butane dihedral angle dynamics in water is dominated by internal friction. *Proc. Natl. Acad. Sci.* **2018**, *115*, 5169–5174.
- [40] Stenger, J.; Madsen, D.; Hamm, P.; Nibbering, E. T.; Elsaesser, T. Ultrafast vibrational dephasing of liquid water. *Phys. Rev. Lett.* **2001**, *87*, 027401.
- [41] Chuntonov, L.; Kumar, R.; Kuroda, D. G. Non-linear infrared spectroscopy of the water bending mode: Direct experimental evidence of hydration shell reorganization? *Phys. Chem. Chem. Phys.* **2014**, *16*, 13172–13181.
- [42] Bertie, J. E.; Lan, Z. Infrared Intensities of Liquids XX: The Intensity of the OH Stretching Band of Liquid Water Revisited, and the Best Current Values of the Optical Constants of H<sub>2</sub>O(l) at 25°C between 15,000 and 1 cm<sup>-1</sup>. *Appl. Spectrosc.* **1996**, *50*, 1047–1057.
- [43] Bertie, J. E.; Ahmed, M. K.; Eysel, H. H. Infrared intensities of liquids. 5. Optical and dielectric constants, integrated intensities, and dipole moment derivatives of H<sub>2</sub>O and D<sub>2</sub>O at 22°C. *J. Phys. Chem.* **1989**, *93*, 2210–2218.
- [44] Silvestrelli, P. L.; Bernasconi, M.; Parrinello, M. Ab initio infrared spectrum of liquid water. *Chem. Phys. Lett.* **1997**, *277*, 478–482.
- [45] Heyden, M.; Sun, J.; Funkner, S.; Mathias, G.; Forbert, H.; Havenith, M.; Marx, D. Dissecting the THz spectrum of liquid water from first principles via correlations in time and space. *Proc. Natl. Acad. Sci.* **2010**, *107*, 12068–12073.
- [46] Schulz, R.; von Hansen, Y.; Daldrop, J. O.; Kappler, J.; Noé, F.; Netz, R. R. Collective hydrogen-bond rearrangement dynamics in liquid water. *J. Chem. Phys.* **2018**, *149*, 244504.
- [47] Habershon, S.; Markland, T. E.; Manolopoulos, D. E. Competing quantum effects in the dynamics of a flexible water model. *J. Chem. Phys.* **2009**, *131*, 024501.
- [48] Marsalek, O.; Markland, T. E. Quantum Dynamics and Spectroscopy of Ab Initio Liquid Water: The Interplay of Nuclear and Electronic Quantum Effects. *J. Phys. Chem. Lett.* **2017**, *8*, 1545–1551.
- [49] Fraley, P. E.; Narahari Rao, K. High resolution infrared spectra of water vapor:  $\nu_1$  and  $\nu_3$  band of H<sub>2</sub><sup>16</sup>O. *J. Mol. Spectrosc.* **1969**, *29*, 348–364.
- [50] McClatchey, R. A.; Benedict, W. S.; Clough, S.; Burch, D.; R.F. C.; Fox, K.; Rothman, L.; Garing, J. S. AFCRL Atmospheric Absorption Line Parameters Compilation. *Environ. Res. Pap.* **1973**,
- [51] Carlson, S.; Brüning, F. N.; Loche, P.; Bonthuis, D. J.; Netz, R. R. Exploring the Absorption Spectrum of Simulated Water from MHz to Infrared. *J. Phys. Chem. A* **2020**, *124*, 5599–5605.
- [52] Zhang, C.; Guidoni, L.; Kühne, T. D. Competing factors on the frequency separation between the OH stretching modes in water. *J. Mol. Liq.* **2015**, *205*, 42–45.
- [53] Schrader, B., Ed. *Infrared and Raman Spectroscopy: Methods and Applications*; Wiley-VCH, 1995.
- [54] Marchesoni, F.; Grigolini, P. On the extension of the Kramers theory of chemical relaxation to the case of nonwhite noise. *J. Chem. Phys.* **1982**, *78*, 6287–6298.
- [55] Morrone, J. A.; Markland, T. E.; Ceriotti, M.; Berne, B. J. Efficient multiple time scale molecular dynamics: Using colored noise thermostats to stabilize resonances. *J. Chem. Phys.* **2011**, *134*, 014103.
- [56] Lee, H. S.; Ahn, S. H.; Darve, E. F. The multi-dimensional generalized Langevin equation for conformational motion of proteins. *J. Chem. Phys.* **2019**, *150*, 174113.
- [57] Ni, Y.; Skinner, J. L. IR and SFG vibrational spectroscopy of the water bend in the bulk liquid and at the liquid-vapor interface, respectively. *J. Chem. Phys.* **2015**, *143*, 014502.
- [58] Medders, G. R.; Paesani, F. Infrared and raman spectroscopy of liquid water through "first-principles" many-body molecular dynamics. *J. Chem. Theory Comput.* **2015**, *11*, 1145–1154.
- [59] Hutter, J.; Iannuzzi, M.; Schiffmann, F.; Vandevondele, J. CP2K: Atomistic simulations of condensed matter systems. *Wiley Interdiscip. Rev. Comput. Mol. Sci.* **2014**, *4*, 15–25.
- [60] VandeVondele, J.; Hutter, J. Gaussian basis sets for accurate calculations on molecular systems in gas and condensed phases. *J. Chem. Phys.* **2007**, *127*, 114105.
- [61] Grimme, S.; Antony, J.; Ehrlich, S.; Krieg, H. A consistent and accurate ab initio parametrization of density functional dispersion correction (DFT-D) for the 94 elements H-Pu. *J. Chem. Phys.* **2010**, *132*, 154104.
- [62] Bussi, G.; Donadio, D.; Parrinello, M. Canonical sampling through velocity rescaling. *J. Chem. Phys.* **2007**, *126*, 014101.
- [63] Kubo, R. Statistical-Mechanical Theory of Irreversible Processes. I. General Theory and Simple Applications to Magnetic and Conduction Problems. *J. Phys. Soc. Japan* **1957**, *12*, 570–586.
- [64] Wiener, N. Generalized Harmonic Analysis. *Acta Math.*

- 1930**, *55*, 117–258.
- [65] Ramírez, R.; López-Ciudad, T.; Kumar P, P.; Marx, D. Quantum corrections to classical time-correlation functions: Hydrogen bonding and anharmonic floppy modes. *J. Chem. Phys.* **2004**, *121*, 3973–3983.

# Time-dependent friction effects on vibrational infrared frequencies and line shapes of liquid water

Florian N. Brünig, Otto Geburtig, Alexander von Canal, Julian Kappler, and Roland R. Netz\*  
*Freie Universität Berlin, Germany*

arXiv:2201.01655v1 [physics.chem-ph] 5 Jan 2022

---

\* rnetz@physik.fu-berlin.de

## I. INFRARED POWER SPECTRA FROM LINEAR-RESPONSE THEORY

Assuming linear response of an observable  $x(t)$  with respect to a force that couples to an observable  $y(t)$ , the response function  $\chi_{xy}(t)$  is related to the correlation function  $C_{xy}(t') = \langle x(t+t')y(t) \rangle$  for  $t \geq 0$  [1]

$$\chi_{xy}(t) = -\frac{1}{k_B T} \frac{d}{dt} C_{xy}(t), \quad (\text{S1})$$

where  $k_B T$  is the thermal energy. Realizing that  $\chi(t)$  is single-sided, i.e.  $\chi(t) = 0$  for  $t < 0$ , the Fourier transform is calculated as

$$\begin{aligned} \tilde{\chi}_{xy}(\omega) &= -\frac{1}{k_B T} \int_{-\infty}^{\infty} dt e^{i\omega t} \frac{d}{dt} C_{xy}(t) \\ \tilde{\chi}_{xy}(\omega) &= -\frac{1}{k_B T} \left( C_{xy}(0) - i\omega \int_0^{\infty} dt e^{i\omega t} C_{xy}(t) \right) \\ \tilde{\chi}_{xy}(\omega) &= -\frac{1}{k_B T} \left( C_{xy}(0) - i\omega \tilde{C}_{xy}^+(\omega) \right), \end{aligned} \quad (\text{S2})$$

where the superscript  $+$  denotes a single-sided Fourier transform. In case of  $x = y$ ,  $C_{xx}(t)$  is an autocorrelation function, which is real and symmetric, therefore it follows for the imaginary part of the response function in Fourier space

$$\tilde{\chi}_{xx}''(\omega) = \frac{1}{k_B T} \omega \text{Re}(\tilde{C}_{xx}^+(\omega)) \quad (\text{S3})$$

$$= \frac{1}{k_B T} \frac{\omega}{2} \tilde{C}_{xx}(\omega). \quad (\text{S4})$$

When computing the power spectra of a stochastic process  $x(t)$ , limited to the time domain  $[0, L_t]$ , the Wiener-Khinchine theorem, eq. (S97) in section XIV, can be used to express  $\tilde{C}_{xx}(\omega)$  in terms of  $\tilde{x}(\omega)$ , turning eq. (S4) into

$$\tilde{\chi}_{xx}''(\omega) = \frac{\omega}{2k_B T L_t} |\tilde{x}(\omega)|^2. \quad (\text{S5})$$

When computing the power spectra of the observable  $x(t)$  from the ensemble average of equilibrium trajectories, a decomposition of  $x(t)$  into two parts  $x(t) = x_1(t) + x_2(t)$  gives rise to three contributions in the total power spectrum

$$\begin{aligned} \omega \tilde{\chi}_{xx}''(\omega) &= \frac{\omega^2}{2k_B T} \left[ \tilde{C}_1(\omega) + \tilde{C}_2(\omega) + 2\tilde{C}_{1,2}(\omega) \right] \\ &= \omega \left[ \tilde{\chi}_1''(\omega) + \tilde{\chi}_2''(\omega) + \tilde{\chi}_{1,2}''(\omega) \right], \end{aligned} \quad (\text{S6})$$

where the cross-correlation contribution  $\tilde{\chi}_{1,2}''(\omega)$  was defined such that it equals the difference spectrum

$$\begin{aligned} \tilde{\chi}_{\text{diff}}''(\omega) &= \tilde{\chi}_{xx}'' - \tilde{\chi}_1''(\omega) - \tilde{\chi}_2''(\omega) = \tilde{\chi}_{1,2}''(\omega) \\ &= \frac{\omega}{k_B T} \tilde{C}_{1,2}(\omega). \end{aligned} \quad (\text{S7})$$

A positive cross-correlation spectrum hints to in-phase motion, a negative cross-correlation spectrum to out-of-phase motion of  $x_1(t+t')$  and  $x_2(t)$  at a given frequency.

In case of  $x(t)$  being the polarization  $\mathbf{p}(t)$  of the system, coupling to an external electric field  $\mathbf{E}(t)$ , the dimensionless dielectric susceptibility  $\chi(t)$  is given by

$$\tilde{\chi}(\omega) = \frac{1}{V \epsilon_0 D} \langle \tilde{\chi}_{\mathbf{p}\mathbf{p}}(\omega) \rangle, \quad (\text{S8})$$

where  $\epsilon_0$  is the vacuum permittivity,  $V$  is the system volume and an average is performed over the  $D$  dimensions of  $\mathbf{p}$ .

## II. DECOMPOSITION OF WATER INFRARED SPECTRA INTO SINGLE-MOLECULAR AND COLLECTIVE COMPONENTS

Fig. S1A and B shows a complete decomposition of the total (nuclear and electronic) IR spectra obtained from aiMD simulations of 256 H<sub>2</sub>O molecules (grey solid lines), as introduced in the main text, into single-molecular (blue solid lines) and collective components (purple solid lines), which follow from the molecular dipole moments  $\mathbf{p}_i(t)$  of all the molecules in the bulk as [2]

$$\tilde{\chi}''_{\text{tot}}(\omega) = \tilde{\chi}''_{\text{mol}}(\omega) + \tilde{\chi}''_{\text{coll}}(\omega) \quad (\text{S9})$$

$$\sim \left\langle \sum_i \mathbf{p}_i(0) \sum_j \mathbf{p}_j(t) \right\rangle = \sum_i \langle \mathbf{p}_i(0) \mathbf{p}_i(t) \rangle + \sum_i \langle \mathbf{p}_i(0) \sum_{j \neq i} \mathbf{p}_j(t) \rangle. \quad (\text{S10})$$

The data clearly shows, that whereas in the OH stretching regime the collective effects are constructive and lead to an amplification of the total infrared spectrum with respect to the single-molecular spectrum, in the HOH bending regime the collective effects are destructive and lead to a slight decrease of the amplitude of the total IR spectrum with respect to the single-molecular spectrum. In the regime of the librations between 300 cm<sup>-1</sup> to 800 cm<sup>-1</sup> the collective effects contribute constructive as well as destructive. At the small signature around 200 cm<sup>-1</sup>, associated with translational vibrations of water molecules against each other, the collective effects contribute constructive.

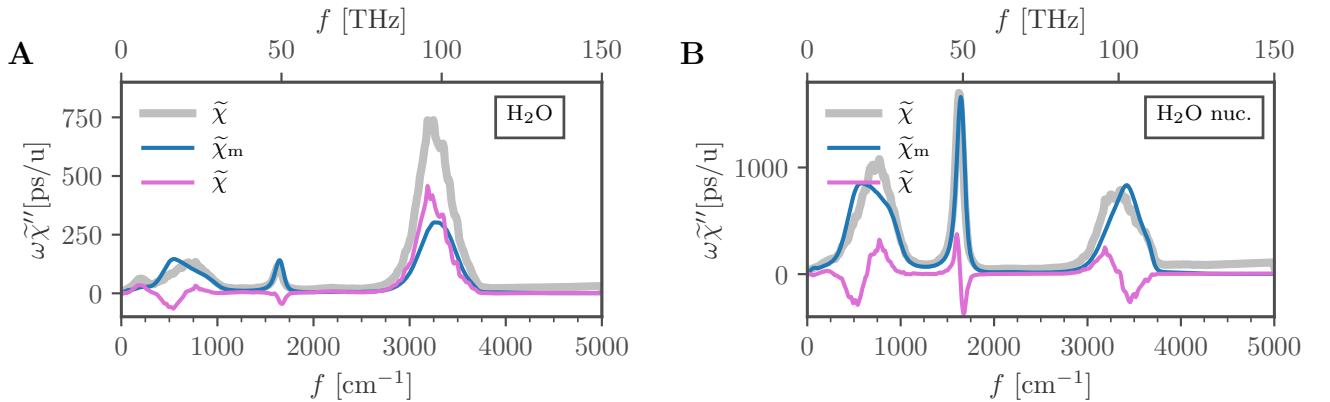


Figure S1. Decomposition of the IR spectra into total (grey solid lines), single-molecular (blue solid lines) and collective contributions (purple solid lines), obtained from the total dipole-moment trajectory from the aiMD simulation of 256 H<sub>2</sub>O molecules including nuclear and electronic charges after Wannier localization (**A**) and an approximation using partial charges on the nuclear dynamics of the same aiMD simulation (**B**, see the following section III for details).

### III. INFRARED SPECTRA FROM NUCLEAR COORDINATES

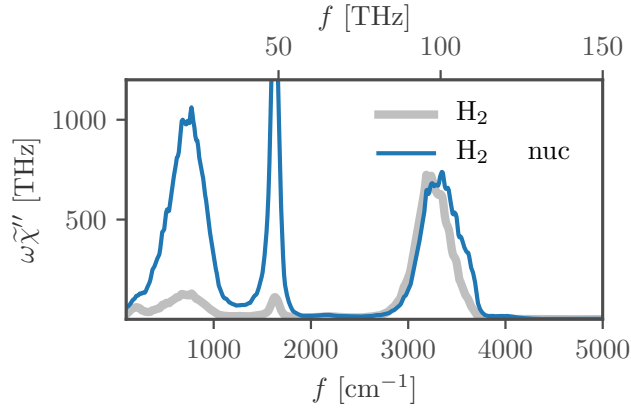


Figure S2. Comparison of IR spectra obtained from the total dipole-moment trajectory including nuclear and electronic charges from the aiMD simulation (grey solid line) and an approximation using partial charges on the nuclear dynamics of the same aiMD simulation (blue solid line).

Fig. S2 shows a comparison of the IR spectrum of the aiMD simulation, using the total dipole moment including nuclear and electronic charges and a nuclei-only power spectrum, which is obtained by assigning the partial charges  $1e$  to the hydrogen atoms and  $-2e$  to the oxygen atoms of the aiMD simulation in post processing. Both spectra are qualitatively similar but the nuclei-only spectrum is significantly increased at lower frequencies, due to the neglect of electronic polarization effects. In the OH-stretching regime at around  $3300\text{ cm}^{-1}$  both spectra coincidentally have a similar amplitude. Interestingly the nuclei-only spectrum is blue-shifted with respect to the spectrum from nuclear and electronic charges, indicating a slow down of the total dipole-moment dynamics in this regime due to the electronic degrees of freedom.



#### IV. EXTRACTION AND PARAMETRIZATION OF THE POTENTIALS

From the entire set of trajectories of a vibrational coordinate a histogram is created with 50 equidistant bins centered at  $x_i$ . From this histogram  $h(x_i)$  the potential (or free energy) is calculated as

$$U(x_i) = -\log(h(x_i))k_B T, \quad (\text{S11})$$

where the potential is shifted vertically so that  $\min(U[x_i]) = 0$ . The largest and smallest value of  $x_i$  where  $U(x_i) < 8k_B T$  are the edges for a new histogram with 99 equidistant bins. From this histogram the potential is again calculated as shown above. This potential is then fitted to a 4th-order polynomial,  $U(x) = a + bx + cx^2 + dx^3 + ex^4$ , using the Levenberg-Marquardt algorithm. The position of the minimum of the fit function,  $x_0$ , is subsequently obtained using Newton's method, both implemented in `scipy v1.5`. Eventually,  $U(x)$  is rewritten as

$$U(x) = k_0 + \frac{k}{2}(x - x_0)^2 + \frac{k_3}{3}(x - x_0)^3 + \frac{k_4}{4}(x - x_0)^4 \quad (\text{S12})$$

$$k_4 = 4e \quad (\text{S13})$$

$$k_3 = 3(d + k_4 x_0) \quad (\text{S14})$$

$$k = 2(c + k_3 x_0 - \frac{6}{4}k_4 x_0^2) \quad (\text{S15})$$

$$k_0 = a - \frac{k_2}{2}x_0^2 + \frac{k_3}{3}x_0^3 - \frac{k_4}{4}x_0^4. \quad (\text{S16})$$

Note that  $k_0$  is small but can be non-zero because of discretization effects. The results of the fits for the different vibrational coordinates are presented in fig. S3A–D, by comparing the second derivatives of the fit functions,  $U''(x) = k + 2k_3(x - x_0) + 3k_4(x - x_0)^2$ , (blue broken lines) with second derivatives obtained numerically from the data,  $U''(x_i) = (U(x_{i+1}) - 2U(x_i) + U(x_{i-1}))/(\Delta x)^2$ , using histograms with 300 equidistant bins. The numerically obtained derivatives are smoothed (grey and purple dots) by iterative convolution with a flat window function, which has a width of three bins. The plots illustrate that for all vibrational coordinates the fit functions and particularly the harmonic fit parameter  $k$  (shown as horizontal grey dotted lines) match well the numerically obtained curvature of the potential around the position of the minima at  $x_0$  (shown as vertical grey dotted lines).

#### V. EXTRACTION OF THE TIME-DEPENDENT FRICTION KERNELS

The extraction of time-dependent friction kernels from trajectories with an anharmonic system potential is performed using a modification of a recently published approach [3] and based on previous work by Harp and Berne [4]. The derivation starts from the generalized Langevin equation (GLE)

$$m\ddot{x}(t) = -\int_0^t \Gamma(t-t')\dot{x}(t')dt' - \nabla U[x(t)] + F_R(t), \quad (\text{S17})$$

which is multiplied by the initial velocity  $\dot{x}(0)$  and ensemble averaged

$$m\langle \dot{x}(0)\ddot{x}(t) \rangle = -\int_0^t dt' \Gamma(t') \langle \dot{x}(0)\dot{x}(t-t') \rangle - \langle \dot{x}(0)\nabla U[x(t)] \rangle, \quad (\text{S18})$$

assuming the random force  $F_R(t)$  to be uncorrelated with  $\dot{x}(0)$ . Defining the correlation functions as

$$C_{vv}(t) = \langle \dot{x}(0)\dot{x}(t) \rangle, \quad (\text{S19})$$

$$C_{v\nabla U}(t) = \langle \dot{x}(0)\nabla U[x(t)] \rangle, \quad (\text{S20})$$

$$C_{x\nabla U}(t) = \langle x(0)\nabla U[x(t)] \rangle, \quad (\text{S21})$$

eq. (S18) is written as

$$m\frac{d}{dt}C_{vv}(t) = -\int_0^t dt' \Gamma(t')C_{vv}(t-t') - C_{v\nabla U}(t), \quad (\text{S22})$$

and integrated over time

$$mC_{vv}(t) - mC_{vv}(0) = -\int_0^t dt' \int_0^{t'} dt'' \Gamma(t')C_{vv}(t''-t') - \int_0^t dt'' C_{v\nabla U}(t''). \quad (\text{S23})$$

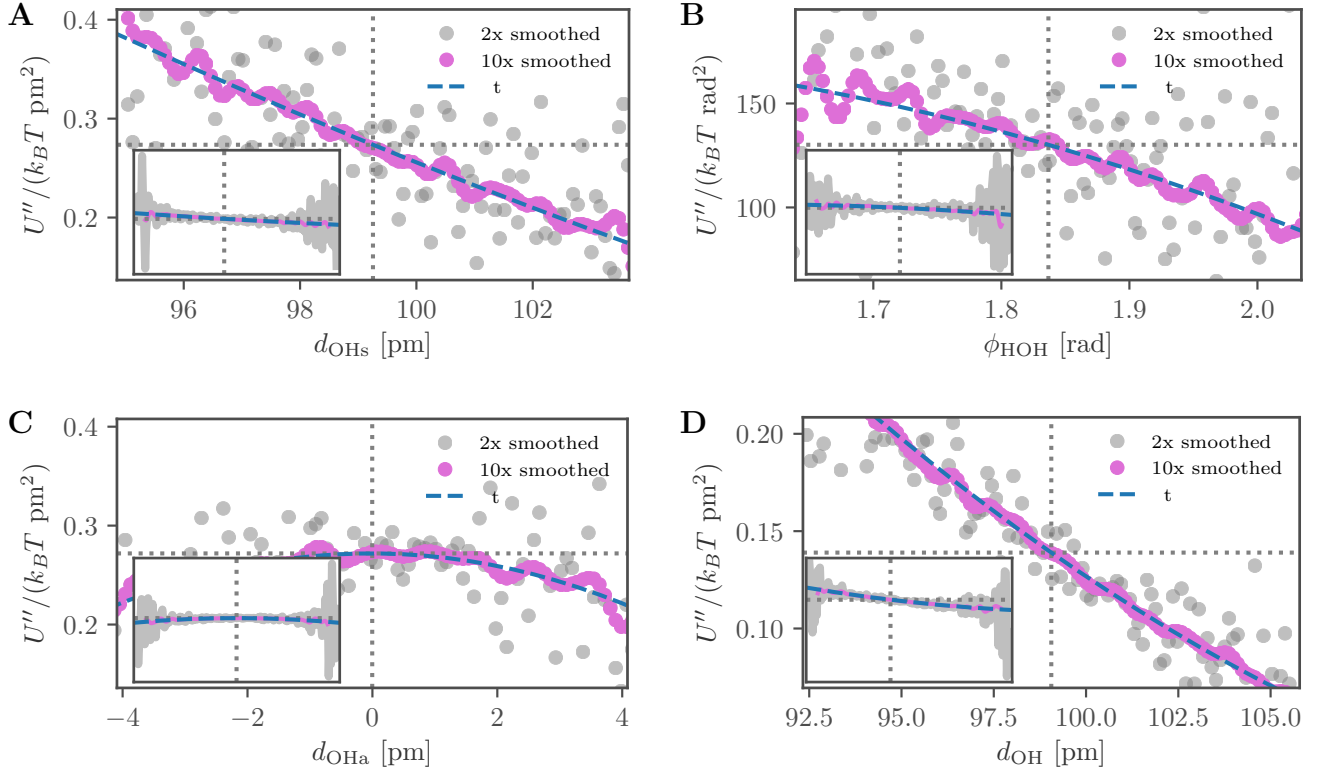


Figure S3. Second derivatives of the potential, obtained numerically and iteratively smoothed (grey and purple dots), of the various vibrational coordinates (**A**:  $d_{\text{OH}_s}$  coordinate, **B**:  $\phi_{\text{HOH}}$  coordinate, **C**:  $d_{\text{OH}_a}$  coordinate and **D**:  $d_{\text{OH}}$  coordinate.). The second derivatives of the fit functions are shown as blue broken lines. The vertical grey dotted lines denote the position of the minima at  $x_0$  and the horizontal grey dotted lines denote the values of the harmonic fit parameters  $k$ . The insets show a wider range of data, for which  $U(x_i) < 8 k_B T$ .

For the terms on the right hand side, one finds

$$\begin{aligned}
\int_0^t dt'' C_{v\nabla U}(t'') &= \int_0^t dt'' \langle \dot{x}(0) \nabla U[x(t'')] \rangle \\
&= \int_0^t dt'' \langle \dot{x}(-t'') \nabla U[x(0)] \rangle \\
&= \left\langle \nabla U[x(0)] \int_0^t dt'' \dot{x}(-t'') \right\rangle \\
&= \left\langle \nabla U[x(0)] \int_{-t}^0 dt'' \dot{x}(t'') \right\rangle \\
&= \langle \nabla U[x(0)] x(0) \rangle - \langle \nabla U[x(0)] x(-t) \rangle \\
&= C_{x\nabla U}(0) - C_{x\nabla U}(t),
\end{aligned} \tag{S24}$$

and

$$\begin{aligned}
\int_0^t dt'' \int_0^{t''} dt' \Gamma(t') C_{vv}(t'' - t') &= \int_0^t dt'' \int_0^{t''} dt''' \Gamma(t'' - t''') C_{vv}(t''') \\
&= \int_0^t dt'' \int_0^{t''} dt''' \Gamma(t'' - t''') C_{vv}(t''') \\
&= \int_0^t dt''' C_{vv}(t''') \int_{t'''}^t dt'' \Gamma(t'' - t''') \\
&= \int_0^t dt''' C_{vv}(t''') \int_0^{t-t'''} dt'' \Gamma(t'') \\
&= \int_0^t dt''' C_{vv}(t''') G(t - t'''), \tag{S25}
\end{aligned}$$

where

$$G(t) = \int_0^t dt' \Gamma(t'), \tag{S26}$$

is the integral over the friction kernel. Inserting eq. (S24) and eq. (S25) into eq. (S23), one obtains

$$mC_{vv}(t) - mC_{vv}(0) = - \int_0^t dt' C_{vv}(t') G(t - t') - C_{x\nabla U}(0) + C_{x\nabla U}(t). \tag{S27}$$

The mass is found to be

$$m = \frac{C_{x\nabla U}(0)}{C_{vv}(0)}, \tag{S28}$$

which follows from multiplying the GLE eq. (S17) by the initial position  $x(0)$ , averaging over the ensemble and evaluating at  $t = 0$

$$m \langle x(0) \ddot{x}(0) \rangle = - \langle x(0) \nabla U[x(0)] \rangle \tag{S29}$$

$$-m \langle \dot{x}(0) \dot{x}(0) \rangle = - \langle x(0) \nabla U[x(0)] \rangle. \tag{S30}$$

Using eq. (S28) in eq. (S27), one finds

$$C_{vv}(t) \frac{C_{x\nabla U}(0)}{C_{vv}(0)} = - \int_0^t dt' C_{vv}(t') G(t - t') + C_{x\nabla U}(t). \tag{S31}$$

Eq. (S31) is a Volterra equation of first kind which can be discretized in time,  $t = i\Delta t$ , and solved numerically,

$$C_{vv}^i \frac{C_{x\nabla U}^0}{C_{vv}^0} = - \sum_{j=0}^i w_{j,i} \Delta t C_{vv}^j G^{i-j} + C_{x\nabla U}^i \tag{S32}$$

$$= -G^i w_{i,i} \Delta t C_{vv}^0 - \sum_{j=0}^{i-1} w_{j,i} \Delta t C_{vv}^j G^{i-j} + C_{x\nabla U}^i, \tag{S33}$$

where  $w_{j,i}$  are integration weights and the corresponding iteration relation reads

$$G^i = - \frac{1}{\omega_{i,i} \Delta t C_{vv}^0} \left( \sum_{j=0}^{i-1} \omega_{i,j} \Delta t C_{vv}^j G^{i-j} + \frac{C_{x\nabla U}^0}{C_{vv}^0} C_{vv}^i - C_{x\nabla U}^i \right). \tag{S34}$$

Thus by calculating the necessary correlation functions,  $C_{vv}^i = C_{vv}(i\Delta t)$  and  $C_{x\nabla U}^i = C_{x\nabla U}(i\Delta t)$ , from equilibrium trajectories, the integral of the time-dependent friction kernel,  $G^i = G(i\Delta t)$ , can be obtained by iteration from the initial value  $G^0 = 0$ . The friction kernel  $\Gamma^i = \Gamma(i\Delta t)$  is subsequently obtained by a numerical derivative.

## VI. POWER SPECTRUM OF THE GENERALIZED LANGEVIN EQUATION

A random process  $x(t)$  with mass  $m$  and subject to time-dependent (or frequency-dependent) friction  $\Gamma(t)$  in a harmonic potential  $U(x) = \frac{k}{2}x^2$  can be described by the generalized Langevin equation

$$m\ddot{x}(t) = - \int_0^t dt' \Gamma(t-t')\dot{x}(t') - kx(t) + F_R(t), \quad (\text{S35})$$

obeying for the random force  $F_R(t)$  the fluctuation-dissipation relation  $\langle F_R(t)F_R(t') \rangle = k_B T \Gamma(t-t')$ . A Fourier transform gives

$$-\omega^2 m \tilde{x}(\omega) = i\omega \tilde{\Gamma}^+(\omega) \tilde{x}(\omega) - k \tilde{x}(\omega) + \tilde{F}_R(\omega), \quad (\text{S36})$$

as well as

$$\begin{aligned} \langle \tilde{F}_R(\omega) \tilde{F}_R(\omega') \rangle &= k_B T \int_{-\infty}^{\infty} dt e^{i\omega t} \int_{-\infty}^{\infty} dt' e^{i\omega' t'} \Gamma(t-t') \\ &= k_B T \int_{-\infty}^{\infty} dt e^{i\omega t} \int_{-\infty}^{\infty} dt' e^{i\omega' t'} \Gamma(t-t') \\ &= k_B T \int_{-\infty}^{\infty} dt' e^{i(\omega'+\omega)t'} \int_{-\infty}^{\infty} dt e^{i\omega(t-t')} \Gamma(t-t') \\ &= 2\pi k_B T \delta(\omega' + \omega) \tilde{\Gamma}(\omega) \end{aligned} \quad (\text{S37})$$

$$= 2\pi k_B T \delta(\omega' + \omega) \tilde{\Gamma}(\omega) \quad (\text{S38})$$

The absorbed power  $\omega \tilde{\chi}''(\omega)$  is derived in Fourier space from linear response to an external force  $F_{\text{ext}}$ , which is calculated according to

$$\tilde{\chi}(\omega) = \frac{\tilde{x}(\omega)}{\tilde{F}_{\text{ext}}(\omega)} \quad (\text{S39})$$

$$= (k - m\omega^2 - i\tilde{\Gamma}^+(\omega)\omega)^{-1}, \quad (\text{S40})$$

and using eqs. (S38) and (S40) the autocorrelation in Fourier space is given by

$$\tilde{C}_{xx}(\omega) = \int_{-\infty}^{\infty} dt e^{i\omega t} \langle x(t)x(0) \rangle \quad (\text{S41})$$

$$\begin{aligned} &= \frac{1}{4\pi^2} \int_{-\infty}^{\infty} dt e^{i\omega t} \int_{-\infty}^{\infty} d\omega' e^{-i\omega' t} \int_{-\infty}^{\infty} d\omega'' e^{-i\omega'' 0} \langle \tilde{x}(\omega') \tilde{x}(\omega'') \rangle \\ &= \frac{1}{4\pi^2} \int_{-\infty}^{\infty} d\omega' 2\pi \delta(\omega - \omega') \int_{-\infty}^{\infty} d\omega'' \langle \tilde{x}(\omega') \tilde{x}(\omega'') \rangle \\ &= \frac{1}{2\pi} \int_{-\infty}^{\infty} d\omega'' \langle \tilde{x}(\omega) \tilde{x}(\omega'') \rangle \end{aligned} \quad (\text{S42})$$

$$\begin{aligned} &= \frac{1}{2\pi} \int_{-\infty}^{\infty} d\omega'' \langle \tilde{\chi}(\omega) \tilde{F}_R(\omega) \tilde{\chi}(\omega'') \tilde{F}_R(\omega'') \rangle \\ &= k_B T \int_{-\infty}^{\infty} d\omega'' \tilde{\chi}(\omega) \tilde{\chi}(\omega'') \delta(\omega'' + \omega) \tilde{\Gamma}(\omega) \\ &= k_B T \tilde{\chi}(\omega) \tilde{\chi}(-\omega) \tilde{\Gamma}(\omega), \end{aligned} \quad (\text{S43})$$

which is further simplified by realizing that the Fourier transform of the purely real function  $\chi(t)$  is even  $\tilde{\chi}(-\omega) = \tilde{\chi}^*(\omega)$

$$\begin{aligned} \tilde{C}_{xx}(\omega) &= k_B T \tilde{\chi}(\omega) \tilde{\chi}^*(\omega) \tilde{\Gamma}(\omega) \\ &= k_B T |\tilde{\chi}(\omega)|^2 \tilde{\Gamma}(\omega) \\ &= \frac{k_B T \tilde{\Gamma}(\omega)}{|k - m\omega^2 - i\tilde{\Gamma}^+(\omega)\omega|^2}. \end{aligned} \quad (\text{S44})$$

From eq. (S4) the power spectrum follows

$$\omega \tilde{\chi}''(\omega) = \frac{\omega^2 \text{Re} \tilde{\Gamma}^+(\omega)}{|k - m\omega^2 - i\tilde{\Gamma}^+(\omega)\omega|^2}. \quad (\text{S45})$$

## VII. POWER SPECTRUM OF THE DAMPED HARMONIC OSCILLATOR

The absorbed power  $\omega\tilde{\chi}''(\omega)$  of the damped harmonic oscillator described by the differential equation

$$m\ddot{x}(t) = -\gamma\dot{x}(t) - kx(t) + F_{\text{ext}}(t), \quad (\text{S46})$$

is computed from the linear response in Fourier space

$$\tilde{\chi}(\omega) = \frac{\tilde{x}(\omega)}{\tilde{F}_{\text{ext}}(\omega)} \quad (\text{S47})$$

$$= (k - m\omega^2 - i\gamma\omega)^{-1} \quad (\text{S48})$$

$$= \frac{k - m\omega^2 + i\gamma\omega}{(k - m\omega^2)^2 + \gamma^2\omega^2}, \quad (\text{S49})$$

where  $\tilde{x}(\omega)$  is the oscillating variable,  $m$  is the mass,  $\gamma$  the friction coefficient,  $k$  the spring constant of the harmonic potential and  $\tilde{F}_{\text{ext}}(\omega)$  an external force. For the power spectrum follows

$$\omega\tilde{\chi}''(\omega) = \frac{\gamma\omega^2}{(k - m\omega^2)^2 + \gamma^2\omega^2}, \quad (\text{S50})$$

which by introducing the time scales  $\tau = 2\gamma/k$ ,  $\tau_\omega = \sqrt{m/k}$  and length scale  $L$  with  $L^2 = 2k_B T/k$  converts to

$$\omega\tilde{\chi}''(\omega) = \frac{L^2}{k_B T} \frac{\tau\omega^2}{4(1 - \tau_\omega^2\omega^2)^2 + \tau^2\omega^2}. \quad (\text{S51})$$

In spectroscopy this is known as a Lorentzian line shape [5], which in the overdamped case,  $\tau_\omega \rightarrow 0$ , reads

$$\omega\tilde{\chi}''(\omega) = \frac{\gamma\omega^2}{k^2 + \gamma^2\omega^2} \quad (\text{S52})$$

$$= \frac{L^2}{k_B T} \frac{\tau\omega^2}{4 + \tau^2\omega^2}. \quad (\text{S53})$$

Eq. (S52) is also known as the Debye line shape.

## VIII. PARAMETRIZATION OF THE EXTRACTED MEMORY KERNELS

The memory kernels  $\Gamma(t)$ , extracted from the aiMD simulation data as described in section V, are truncated at 50 ps, over-sampled at a time resolution of  $\Delta t = 0.025$  fs and subsequently Fourier transformed using the FFT algorithm implemented in numpy v1.19. The real part of the Fourier-transformed memory kernel is then fitted to a combination of  $n$  exponential and  $l$  oscillating memory kernels according to eq. (5) in the main text. The Fourier-transformed expressions of the fundamental kernels are found to be

$$\tilde{\Gamma}_{\text{osc}}^+(\omega, a_i, \tau_i, \omega_i) = \frac{a_i}{2} \left( \frac{1 + \frac{i}{\omega_i\tau_i}}{\frac{1}{\tau_i} + i\omega_i - i\omega} + \frac{1 - \frac{i}{\omega_i\tau_i}}{\frac{1}{\tau_i} - i\omega_i - i\omega} \right) \quad (\text{S54})$$

$$\tilde{\Gamma}_{\text{exp}}^+(\omega, \gamma_i, \tau_i) = \gamma_i \frac{1}{1 - i\omega\tau_i} \quad (\text{S55})$$

$$\tilde{\Gamma}^+(\omega) = \sum_{i=1}^n \tilde{\Gamma}_{\text{exp}}^+(\omega, \gamma_i, \tau_i^e) + \sum_{i=1}^l \tilde{\Gamma}_{\text{osc}}^+(\omega, a_i, \tau_i^o, \omega_i) \quad (\text{S56})$$

The real part of the Fourier-transformed memory kernel  $\tilde{\Gamma}^+(\omega)$  is fitted in the  $(2n + 3l)$ -dimensional parameter space using the Levenberg-Marquardt algorithm implemented in scipy v1.5.  $n$  and  $l$  are iteratively increased until the fit quality does not improve significantly. The initial values for all  $\gamma_i$ ,  $\tau_i^e$ ,  $a_i$ ,  $\tau_i^o$  and  $\omega_i$  are chosen suitably. After fitting in Fourier space, another fit is performed in the time domain, by subtracting the  $l$  oscillating fit functions from the memory kernels in the time domain and again fitting the  $n$  exponential functions to the remainder. This significantly improves the fits for the long-time tails of the memory kernels. The hereby obtained fit parameters for the friction memory kernels for the different vibrational coordinates in the bulk water system are summarized in tabs. S1–S4.

Table S1. Fit parameters according to eq. (5) in the main text of the friction memory kernel of the  $d_{\text{OHs}}$  coordinate.

$\gamma_i$ [u/ps]	$\tau_i^e$ [ps]		
2758	0.115		
25941	1.28		
54005	5.72		
$a_i$ [u/ps <sup>2</sup> ]	$\tau_i^o$ [ps]	$\omega_i$ [THz]	
8468	0.00944	170	
3525	0.0146	1290	
5985	0.0256	614	
1095	0.0599	675	
10560	0.0807	28.7	
6318	0.122	313	

Table S2. Fit parameters according to eq. (5) in the main text of the friction memory kernel of the  $\phi_{\text{HOH}}$  coordinate.

$\gamma_i$ [u/ps]	$\tau_i^e$ [ps]		
661	0.582		
5210	3.08		
$a_i$ [u/ps <sup>2</sup> ]	$\tau_i^o$ [ps]	$\omega_i$ [THz]	
322	0.0257	1280	
2139	0.0283	28.9	
2577	0.0322	953	
37	0.0323	1590	
786	0.0394	110	
4600	0.0396	643	
374	0.0417	162	
435	0.0465	136	
4089	0.0532	612	
69	0.056	252	
471	0.0612	84.4	
49	0.0839	284	
40	0.12	311	
2836	0.143	14.4	

Table S3. Fit parameters according to eq. (5) in the main text of the friction memory kernel of the  $d_{\text{OHa}}$  coordinate.

$\gamma_i$ [u/ps]	$\tau_i^e$ [ps]		
5653	0.183		
32596	2.03		
$a_i$ [u/ps <sup>2</sup> ]	$\tau_i^o$ [ps]	$\omega_i$ [THz]	
7584	0.0165	1280	
3186	0.021	300	
5051	0.0266	602	
3208	0.0361	141	
1320	0.0401	413	
2810	0.0415	644	
39665	0.0752	36.5	
1353	0.0768	677	
2010	0.0856	100	

Table S4. Fit parameters according to eq. (5) in the main text of the friction memory kernel of the  $d_{\text{OH}}$  coordinate.

$\gamma_i$ [u/ps]	$\tau_i^e$ [ps]	
1212	0.109	
9005	1.06	
19399	4.52	
$a_i$ [u/ps <sup>2</sup> ]	$\tau_i^o$ [ps]	$\omega_i$ [THz]
1343	0.0174	249
1669	0.0264	616
1544	0.0301	145
420	0.0364	411
137	0.0688	673
845	0.0699	100
10641	0.081	35.5
1802	0.115	312

## IX. SIMULATION OF THE GENERALIZED LANGEVIN EQUATION

The GLE

$$m\ddot{x}(t) = - \int_0^t \Gamma(t-t')\dot{x}(t')dt' - \nabla U[x(t)] + F_R(t), \quad (\text{S57})$$

with a sum of  $n$  exponential and  $l$  oscillating memory kernels, analogous to eq. (5) in the main text,

$$\Gamma(t) = \sum_{i=1}^n a_i e^{-t/\tau_i} + \sum_{i=1}^l a_i e^{-t/\tau_i} \left( \cos(\omega_i t) + \frac{1}{\tau_i \omega_i} \sin(\omega_i t) \right), \quad (\text{S58})$$

can be efficiently simulated using a Markovian embedding (which for the oscillating components is derived in detail in section X)

$$\dot{x}(t) = v(t) \quad (\text{S59})$$

$$m_x \dot{v}(t) = -\nabla U[x(t)] + \sum_{i=1}^n a_i [y_i(t) - x(t)] + \sum_{i=1}^l a_i [z_i(t) - x(t)] \quad (\text{S60})$$

$$\gamma_i \dot{y}_i(t) = a_i [x(t) - y_i(t)] + F_i(t) \quad \text{for } n \text{ exp. components} \quad (\text{S61})$$

$$\dot{z}_i(t) = w_i(t) \quad (\text{S62})$$

$$m_i \dot{w}_i(t) = -\gamma_i w_i(t) + a_i [x(t) - z_i(t)] + F_i(t) \quad \text{for } l \text{ osc. components} \quad (\text{S63})$$

For the  $n$  exponential components we obtain  $a_i = \frac{\gamma_i}{\tau_i^e}$  from the fit parameters  $\gamma_i$  and  $\tau_i^e$ . To get  $m_i$  and  $\gamma_i$  for the  $l$  oscillating components from the fit parameters  $a_i$ ,  $\tau_i^o$  and  $\omega_i$  we use

$$m_i = a_i ((\tau_i^o)^{-2} + \omega_i^2)^{-1} \quad (\text{S64})$$

$$\gamma_i = 2 \frac{m_i}{\tau_i^o} \quad (\text{S65})$$

The random force  $F_i$  present in eqs. (S61) and (S63) is

$$F_i = \sqrt{2k_B T \gamma_i \delta t^{-1}} \Xi \quad (\text{S66})$$

Where  $\Xi$  is a Gaussian random distribution with zero mean and a standard deviation of one. In the numerical simulation we use the `numpy.random.normal` function to generate these random numbers. Eqs. (S60)–(S63) are numerically solved using a 4th-order Runge-Kutta scheme to get the trajectory of  $x$ . The timestep of the simulation is  $1 \times 10^{-6}$  ps and only every 500th value is stored. Thus the trajectory is evaluated at a time step of 0.5 fs. The trajectory contains  $2.5 \times 10^7$  values which corresponds to a simulation time of  $1.25 \times 10^4$  ps. Each trajectory is divided into 50 parts of 250 ps and their spectra are calculated using the Wiener-Kintchine relation introduced in section XIV. All 50 spectra are then averaged to give the final spectrum. Starting velocity and position were set to be zero.

The memoryless Langevin equation, with a friction constant  $\gamma$  replacing the integral over the memory kernel

$$m\ddot{x}(t) = -\gamma\dot{x}(t) - \nabla U[x(t)] + F_R(t), \quad (\text{S67})$$

is likewise simulated using a 4th-order Runge-Kutta scheme. The timestep of these simulations is 0.1 fs for a total of  $10^7$  steps, which corresponds to a simulation time of 1000 ps. Each trajectory is divided into 200 parts of 5 ps and their spectra are calculated using the Wiener-Kintchine relation introduced in section XIV. All 200 spectra are then averaged to give the final spectrum.

## X. OSCILLATING MEMORY KERNELS

### A. Oscillating memory kernels from Hamiltonian

Oscillating memory kernels arise from inertial dynamics in orthogonal degrees of freedom at time scales of the order of the primary reaction coordinate. The relation of the time scales of the orthogonal coordinate and the memory kernel is



understood from an explicit derivation of the dynamics of the primary coordinate  $x$  with velocity  $v$ , linearly coupled to an orthogonal coordinate  $y$  with velocity  $w$  and coupling constant  $k$ . The Hamiltonian of the system is given as

$$H = \frac{m}{2}v^2 + \frac{m_y}{2}w^2 + \frac{k}{2}(x - y)^2, \quad (\text{S68})$$

defining the Hamilton equations

$$\dot{x}(t) = v \quad (\text{S69})$$

$$m\dot{v}(t) = k[x(t) - y(t)] \quad (\text{S70})$$

$$\dot{y}(t) = w(t) \quad (\text{S71})$$

$$m_y\dot{w}(t) = -k[x(t) - y(t)]. \quad (\text{S72})$$

These Newtonian equations of motion can straight-forwardly be extended to Langevin equations by introducing random forces  $F_x(t)$ ,  $F_y(t)$  and friction terms with coefficients  $\gamma_x, \gamma_y$

$$\dot{x}(t) = v \quad (\text{S73})$$

$$m\dot{v}(t) = -\gamma_x v(t) + k[x(t) - y(t)] + F_x(t) \quad (\text{S74})$$

$$\dot{y}(t) = w(t) \quad (\text{S75})$$

$$m_y\dot{w}(t) = -\gamma_y w(t) - k[x(t) - y(t)] + F_y(t). \quad (\text{S76})$$

The random forces are designed to introduce dynamics on the order of  $k_B T$  but no net energy transfer into the system. Therefore they have zero mean,  $\langle F_i(t) \rangle = 0$ , and their strength on the order of the friction forces  $\langle F_i(t)F_i(t') \rangle = 2\gamma_i k_B T \delta(t - t')$ , fulfilling the fluctuation-dissipation relation.

To obtain the GLE including the memory kernel we will now find a solution for  $y$  using eq. (S76) and insert this solution in eq. (S74). Eq. (S76) is essentially a driven damped harmonic oscillator, which can be solved in a general fashion using matrix exponentials and introducing the inertial time scale  $\tau_{m_y} = m_y/\gamma_y$  and the memory time scale  $\tau_{k_y} = \gamma_y/k$ . First we write the coupled first order ordinary differential eqs. (S75) and (S76) in the matrix form

$$\dot{\vec{y}}(t) = A\vec{y}(t), \quad (\text{S77})$$

where

$$\vec{y}(t) = \begin{pmatrix} y \\ \dot{y} \end{pmatrix} \quad (\text{S78})$$

$$A = \begin{pmatrix} 0 & 1 \\ -(\tau_{m_y}\tau_{k_y})^{-1} & -\tau_{m_y}^{-1} \end{pmatrix}, \quad (\text{S79})$$

$$A^{-1} = \begin{pmatrix} -\tau_{m_y}^{-1} & (\tau_{m_y}\tau_{k_y})^{-1} \\ -1 & 0 \end{pmatrix}. \quad (\text{S80})$$

The solution is given as

$$\begin{aligned} \vec{y}(t) &= \exp(A[t - t_0])\vec{y}_0 \\ &+ \int_{t_0}^t dt' \exp(A[t - t']) \begin{pmatrix} 0 \\ -(\tau_{m_y}\tau_{k_y})^{-1}x(t') + m_y^{-1}F_y(t') \end{pmatrix}, \end{aligned} \quad (\text{S81})$$

Next a partial integration over the integral containing  $x(t)$  is performed

$$\begin{aligned} \vec{y}(t) &= \exp(A[t - t_0])\vec{y}_0 \\ &- \left[ A^{-1} \exp(A[t - t']) \begin{pmatrix} 0 \\ -(\tau_{m_y}\tau_{k_y})^{-1}x(t') \end{pmatrix} \right]_{t_0}^t \\ &+ A^{-1} \int_{t_0}^t dt' \exp(A[t - t']) \begin{pmatrix} 0 \\ -(\tau_{m_y}\tau_{k_y})^{-1}v(t') \end{pmatrix} \\ &+ \int_{t_0}^t dt' \exp(A[t - t']) \begin{pmatrix} 0 \\ m_y^{-1}F_y(t') \end{pmatrix}. \end{aligned} \quad (\text{S82})$$

The matrix exponential can be evaluated by diagonalizing the matrix  $A$ . After introducing  $\omega_0 = \sqrt{(2\tau_{m_y})^{-2} - (\tau_{m_y}\tau_{k_y})^{-1}}$  the Eigenvalues  $\lambda_{1,2}$  of  $A$  are given as

$$\lambda_{1,2} = -(2\tau_{m_y})^{-1} \pm \omega_0, \quad (\text{S83})$$

and the matrix exponential reads

$$\exp(At) = \frac{1}{\lambda_2 - \lambda_1} \begin{pmatrix} \lambda_2 e^{\lambda_1 t} - \lambda_1 e^{\lambda_2 t} & e^{\lambda_2 t} - e^{\lambda_1 t} \\ \lambda_1 \lambda_2 (e^{\lambda_1 t} - e^{\lambda_2 t}) & \lambda_2 e^{\lambda_2 t} - \lambda_1 e^{\lambda_1 t} \end{pmatrix} \quad (\text{S84})$$

$$= e^{-t/(2\tau_{m_y})} \begin{pmatrix} \cosh(\omega_0 t) + \frac{\sinh(\omega_0 t)}{2\tau_{m_y}\omega_0} & -\frac{\sinh(\omega_0 t)}{\omega_0} \\ \frac{\sinh(\omega_0 t)}{\tau_{m_y}\tau_{k_y}\omega_0} & \cosh(\omega_0 t) - \frac{\sinh(\omega_0 t)}{2\tau_{m_y}\omega_0} \end{pmatrix}, \quad (\text{S85})$$

giving

$$A^{-1} \exp(At) = \tau_{m_y}\tau_{k_y} e^{-t/(2\tau_{m_y})} \begin{pmatrix} -\frac{1}{\tau_{m_y}} \cosh(\omega_0 t) + \frac{1}{2\tau_{m_y}^2\omega_0} \sinh(\omega_0 t) + \frac{1}{\tau_{m_y}\tau_{k_y}\omega_0} \sinh(\omega_0 t) & -\frac{1}{2\tau_{m_y}\omega_0} \sinh(\omega_0 t) - \cosh(\omega_0 t) \\ \frac{1}{\tau_{m_y}\tau_{k_y}} \cosh(\omega_0 t) + \frac{1}{\tau_{m_y}\tau_{k_y}\omega_0} \sinh(\omega_0 t) & \frac{1}{\tau_{m_y}\tau_{k_y}\omega_0} \sinh(\omega_0 t) \end{pmatrix}. \quad (\text{S86})$$

The solution for  $y(t) = \bar{y}_1(t)$  is now obtained from eqs. (S82)–(S86) and by sending  $t_0 \rightarrow -\infty$ , i.e. assuming an equilibrated system

$$y(t) = x(t) - \int_{-\infty}^t dt' v(t') e^{-(t-t')/(2\tau_{m_y})} \left[ \cosh(\omega_0(t-t')) + \frac{1}{2\tau_{m_y}\omega_0} \sinh(\omega_0(t-t')) \right] - \int_{-\infty}^t dt' m_y^{-1} F_y(t') e^{-(t-t')/(2\tau_{m_y})} \frac{1}{\omega_0} \sinh(\omega_0(t-t')). \quad (\text{S87})$$

To obtain the generalized Langevin equation for  $x(t)$  containing the oscillating memory kernel

$$\Gamma(t) = k e^{-t/(2\tau_{m_y})} \left[ \cosh(\omega_0 t) + \frac{1}{2\tau_{m_y}\omega_0} \sinh(\omega_0 t) \right], \quad (\text{S88})$$

eq. (S87) is inserted in eq. (S74)

$$m\dot{v}(t) = -\gamma_x v(t) + F_x(t) + \int_{-\infty}^t dt' v(t') \Gamma(t-t') + F'_y(t). \quad (\text{S89})$$

### B. Underdamped limit: oscillating kernel

The kernel of eq. (S88) can be analysed for two limiting cases. For  $\text{Im}(\omega_0) > (2\tau_{m_y})^{-1}$ , which is equivalent to  $4\tau_{m_y} > \tau_{k_y}$ , the underdamped case,  $\omega_0$  is purely imaginary and the kernel is

$$\Gamma(t) = k e^{-t/(2\tau_{m_y})} \cos(\text{Im}(\omega_0)t) + \frac{1}{2\tau_{m_y}\text{Im}(\omega_0)} \sin(\text{Im}(\omega_0)t). \quad (\text{S90})$$

The integral is evaluated to

$$\gamma = \int_0^\infty dt \Gamma(t) = k \frac{4\tau_{m_y}}{1 - 4\tau_{m_y}^2 \text{Im}(\omega_0)^2} = k\tau_{k_y} = \gamma_y, \quad (\text{S91})$$

### C. Overdamped limit: exponential kernel

For  $\text{Re}(\omega_0) < (4\tau_{m_y})^{-1}$  and  $\tau_{k_y} > (4\tau_{m_y})$ , the overdamped case, it follows that  $\omega_0$  is purely real. The integral equally gives

$$\gamma = \int_0^\infty dt \Gamma(t) = k \frac{4\tau_{m_y}}{1 - 4\tau_{m_y}^2 \omega_0^2} = k\tau_{k_y} = \gamma_y. \quad (\text{S92})$$

## XI. DECOMPOSITION OF THE OH STRETCH MODE

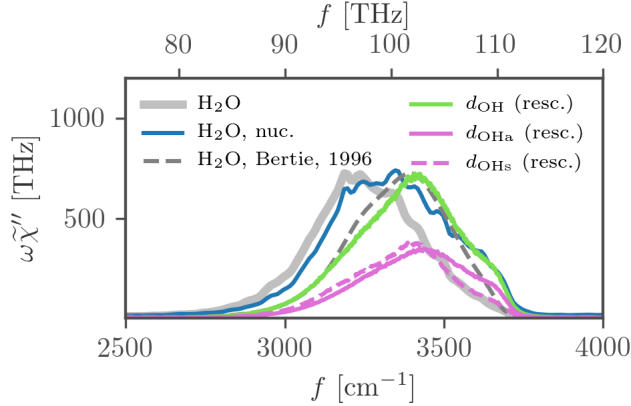


Figure S4. Comparison of IR spectra in the OH-stretching regime obtained from the total dipole-moment trajectory including nuclear and electronic charges from the aiMD simulation of 256 H<sub>2</sub>O molecules (grey solid line), an approximation using partial charges on the nuclear dynamics of the same aiMD simulation (blue solid line, introduced in section III), experimental FTIR data (grey broken line) [6] and rescaled power spectra of the  $d_{\text{OH}}$  (green solid line),  $d_{\text{OHs}}$  (purple solid line) and  $d_{\text{OHa}}$  (purple broken line) vibrational coordinates.

As introduced in the main text, vibrational coordinates for the OH stretch mode are given by  $d_{\text{OHs}} = (d_{\text{OH1}} + d_{\text{OH2}})/2$  for the symmetric stretching-vibration and  $d_{\text{OHa}} = (d_{\text{OH1}} - d_{\text{OH2}})/2$  for the anti-symmetric stretching vibration. Fig. S4 compares the power spectra of these coordinates, obtained from averaging over all 256 H<sub>2</sub>O molecules in the aiMD simulation, to power spectra of the  $d_{\text{OH}}$  coordinate, experimental FTIR data and the IR spectra obtained from the total dipole-moment trajectory including nuclear and electronic charges from the aiMD simulation and an approximation using partial charges on the nuclear dynamics of the aiMD simulation, as introduced in section III. The power spectrum of the  $d_{\text{OH}}$  coordinate is blue-shifted with respect to the power spectra considering the total dipole moment, indicating a slow down of the collective nuclear and electronic dynamics with respect to the single-molecule dynamics, as discussed in section II. This could be similar to the effect of the slow down observed in the IR spectra including electronic degrees of freedom compared to the nuclei-only IR spectra, discussed in section III. As expected for the decomposition, the power spectra of  $d_{\text{OHs}}$  and  $d_{\text{OHa}}$  exactly sum up to the  $d_{\text{OH}}$  power spectrum, there exists no remaining cross-correlation spectrum, so they form orthogonal coordinates.

The effective masses of the coordinates are determined by the equipartition theorem  $m_{\text{OH-sy.}} = k_B T / \langle \dot{d}_{\text{OHs}}^2 \rangle = 1.90104 \text{ u}$ ,  $m_{\text{OH-as.}} = k_B T / \langle \dot{d}_{\text{OHa}}^2 \rangle = 1.84571 \text{ u}$  and  $m_{\text{OH}} = k_B T / \langle \dot{d}_{\text{OH}}^2 \rangle = 0.936477 \text{ u}$ . Analytic estimates are determined by the reduced mass of the  $d_{\text{OH}}$  coordinate  $m_{\text{OH}} = (m_{\text{O}} m_{\text{H}}) / (m_{\text{O}} + m_{\text{H}}) = 0.947617 \text{ u}$ . It follows for the masses of the  $d_{\text{OHs}}$  and  $d_{\text{OHa}}$  coordinates  $m_{\text{OH-sy.}} = m_{\text{OH-as.}} = 2m_{\text{OH}} = 1.89523 \text{ U}$ .

The potentials, power spectra and analysis in terms of frequency-dependent friction of the  $d_{\text{OHs}}$  and  $\phi_{\text{HOH}}$  coordinates are shown in the main text. The remaining discussion is shown here for the  $d_{\text{OH}}$  coordinate in fig. S5 and for the  $d_{\text{OHa}}$  coordinate in fig. S6. The potential of the  $d_{\text{OH}}$  coordinate shows strong non-harmonic contributions in fig. S5A, seen from the reduced potential coefficients  $\tilde{k}_3 = k_3 / k_B T (k / k_B T)^{-3/2} = -0.128$  and  $\tilde{k}_4 = k_4 / k_B T (k / k_B T)^{-2} = 0.00503$ . The potential of the  $d_{\text{OHa}}$  coordinate is symmetric by definition and therefore has a negligible cubic and only a small quartic contribution  $\tilde{k}_4 = -0.0141$  in fig. S6A, when comparing to the potential of the  $d_{\text{OHs}}$  coordinate, shown in fig. 3A in the main text to have a significant cubic contribution. When compared to the potential of a single water molecule in figs. S5B and S6B, the  $d_{\text{OH}}$  coordinate shows a shift of the minimum from 97.37 pm to 99.06 pm, i.e. elongation of the bond length due to hydrogen bonding. As expected the potential of  $d_{\text{OHa}}$  coordinate is centered around zero for both systems. Both coordinates show a significant potential softening in the liquid phase, which follows from comparison of the dominant harmonic contributions of  $k / (k_B T) = 0.139 \text{ pm}^{-2}$  for  $d_{\text{OH}}$  and  $k / (k_B T) = 0.272 \text{ pm}^{-2}$  for  $d_{\text{OHa}}$  with the respective gas-phase values of  $k / (k_B T) = 0.183 \text{ pm}^{-2}$  for  $d_{\text{OH}}$  and  $k / (k_B T) = 0.352 \text{ pm}^{-2}$  for  $d_{\text{OHa}}$ .

The memory kernels in the time domain, shown in figs. S5C for the  $d_{\text{OH}}$  coordinate and S6C for the  $d_{\text{OHa}}$  coordinate, are discussed further below in fig. S7. The frequency-dependent friction, shown in figs. 3D in the main text for the  $d_{\text{OHs}}$  coordinate, S5D for the  $d_{\text{OH}}$  coordinate and S6D for the  $d_{\text{OHa}}$  coordinate show remarkable differences. The frequency-dependent friction of the  $d_{\text{OHs}}$  coordinate shows a much stronger contribution in the regime of the HOH bending band at around  $1650 \text{ cm}^{-1}$ , indicating that it couples more intensely to the HOH bending mode than the

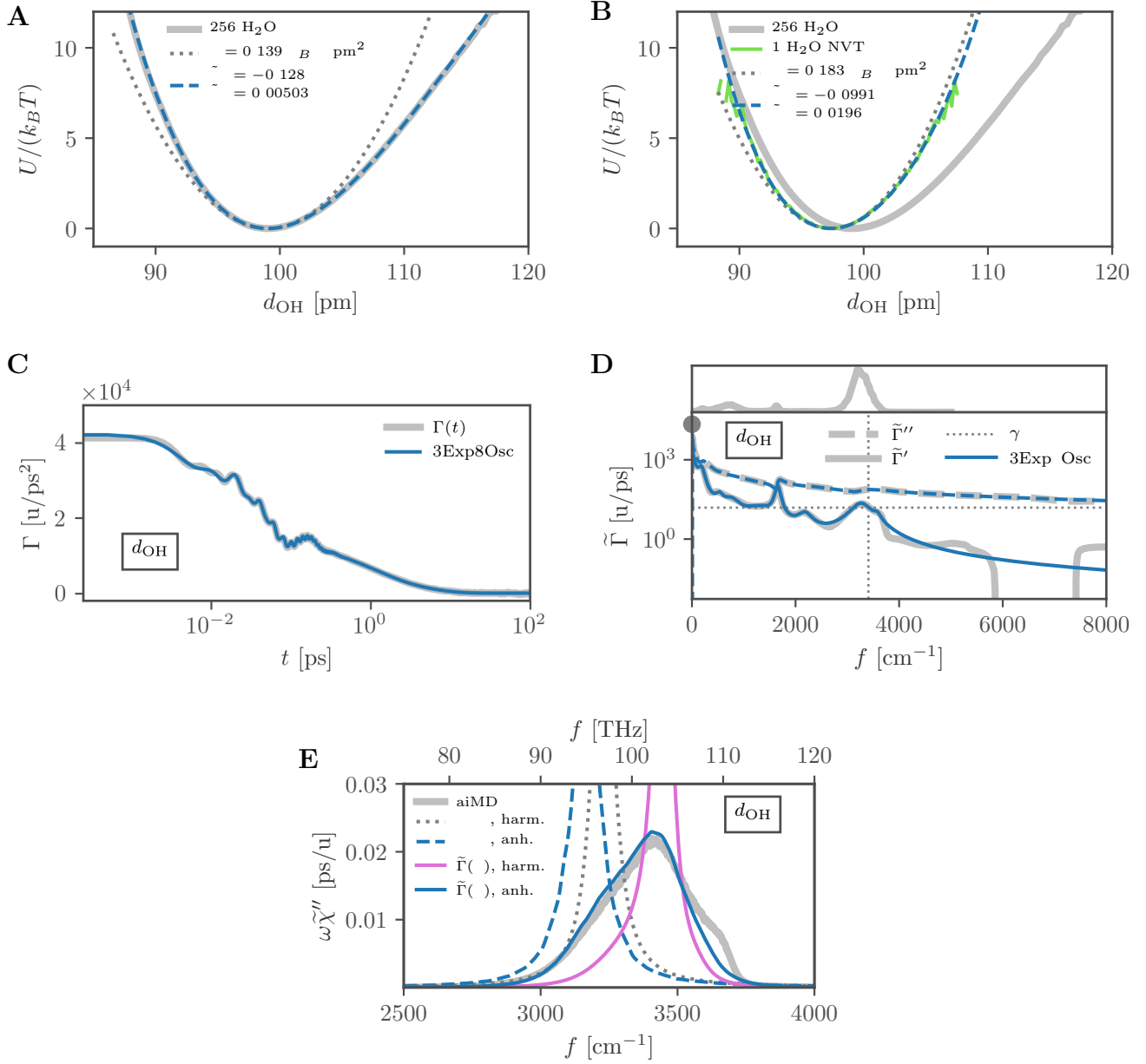


Figure S5. Results for the stretch coordinate  $d_{\text{OH}}$  from aiMD simulations. **A, B:** Potential  $U(d_{\text{OH}})$  for 256 H<sub>2</sub>O in the liquid phase (grey solid line) and for a single H<sub>2</sub>O (green solid line in B), both compared to the non-harmonic fit according to eq. (4) in the main text (blue broken line) and the harmonic part (grey dotted line). **C, D:** Friction as a function of time and frequency (grey lines) compared with the fit according to eq. (5) in the main text (blue lines). Real and imaginary parts in (D) are shown as solid and broken lines, the spectrum on top is the full absorption spectrum from aiMD. The dotted horizontal line in (D) shows the constant real friction  $\gamma_{\text{OH}} = \tilde{\Gamma}'(f_{\text{OH}})$  evaluated at the OH stretch vibrational frequency  $f_{\text{OH}} = 3400$  cm<sup>-1</sup>. The grey circle denotes the static friction  $\tilde{\Gamma}'(0)$ . **E:** Power spectrum  $\omega \tilde{\chi}''$  (grey solid line) compared to models of varying complexity: Lorentzian with harmonic potential and constant friction  $\gamma_{\text{OH}}$  (grey dotted line), non-harmonic potential and constant friction  $\gamma_{\text{OH}_s}$  (blue broken line), harmonic potential and frequency-dependent friction  $\tilde{\Gamma}(f)$  (purple solid line), non-harmonic potential and frequency-dependent friction  $\tilde{\Gamma}(f)$  (blue solid line).

$d_{\text{OH}_a}$  mode.

Figs. S5E and S6E show the power spectra of the two coordinates, compared to the different GLE models. As shown in the main text already for the  $d_{\text{OH}_s}$  and  $\phi_{\text{HOH}}$  coordinates, the frequency-dependent-friction model including a non-harmonic potential outperforms the other models for all coordinates. In case of the  $d_{\text{OH}_a}$  coordinate, shown in fig. S6E, the frequency-dependent-friction model with the harmonic potential also performs very well, due to the negligible non-harmonic contribution to the potential in fig. S6A.

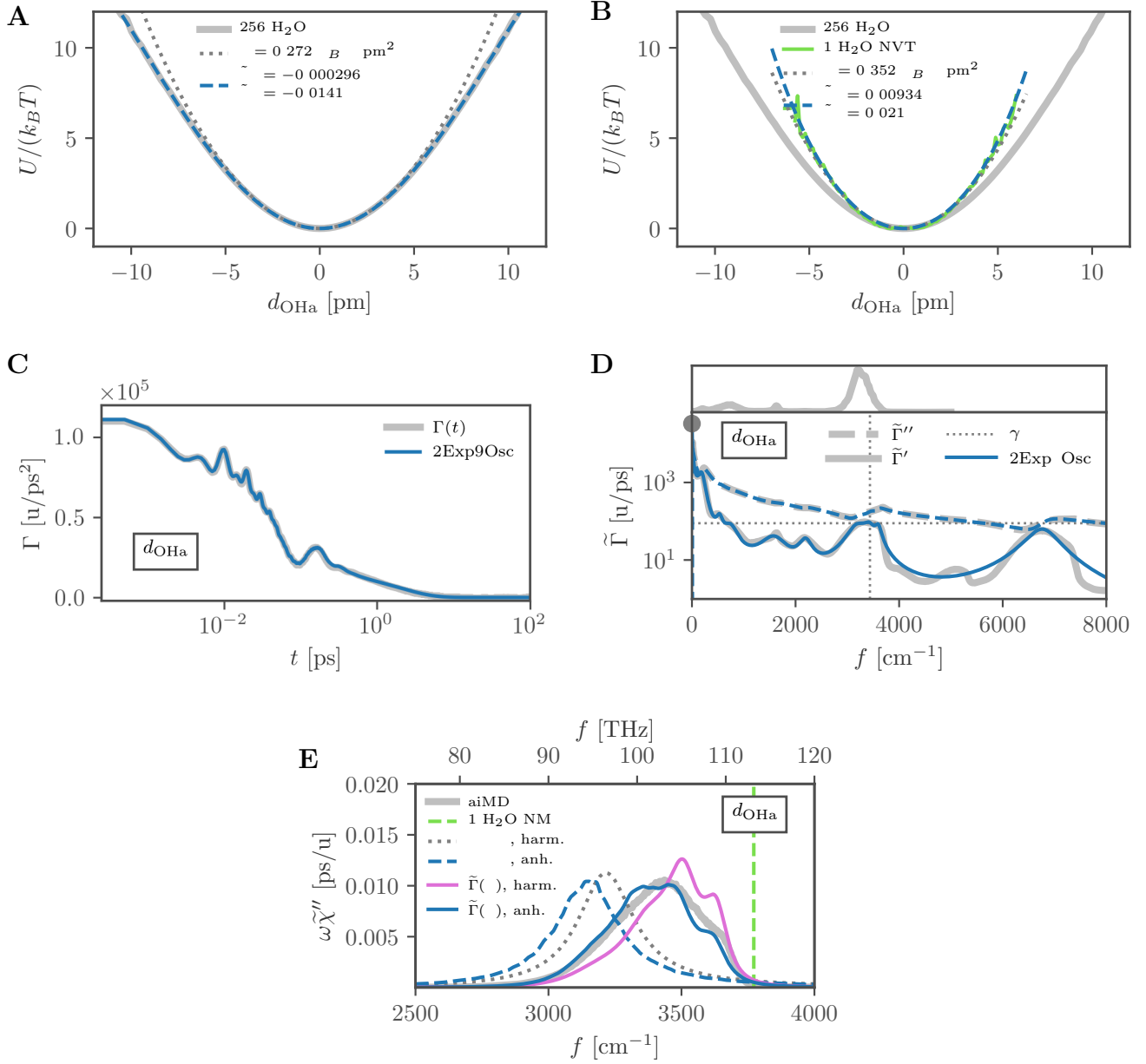


Figure S6. Results for the anti-symmetric stretch coordinate  $d_{\text{OHa}}$  from aiMD simulations. **A, B:** Potential  $U(d_{\text{OHa}})$  for 256 H<sub>2</sub>O in the liquid phase (grey solid line) and for a single H<sub>2</sub>O (green solid line in B), both compared to the non-harmonic fit according to eq. (4) in the main text (blue broken line) and the harmonic part (grey dotted line). **C, D:** Friction as a function of time and frequency (grey lines) compared with the fit according to eq. (5) in the main text (blue lines). Real and imaginary parts in (D) are shown as solid and broken lines, the spectrum on top is the full absorption spectrum from aiMD. The dotted horizontal line in (D) shows the constant real friction  $\gamma_{\text{OHa}} = \tilde{\Gamma}'(f_{\text{OHa}})$  evaluated at the OH stretch vibrational frequency  $f_{\text{OHa}} = 3440 \text{ cm}^{-1}$ . The grey circle denotes the static friction  $\tilde{\Gamma}'(0)$ . **E:** Power spectrum  $\omega \tilde{\chi}''$  (grey solid line) compared to models of varying complexity: normal mode of single H<sub>2</sub>O (broken vertical line), Lorentzian with harmonic potential and constant friction  $\gamma_{\text{OHa}}$  (grey dotted line), non-harmonic potential and constant friction  $\gamma_{\text{OHa}}$  (blue broken line), harmonic potential and frequency-dependent friction  $\tilde{\Gamma}(f)$  (purple solid line), non-harmonic potential and frequency-dependent friction  $\tilde{\Gamma}(f)$  (blue solid line).

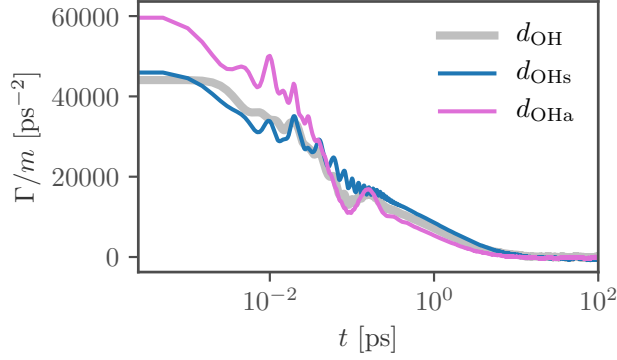


Figure S7. Comparison of time-dependent friction kernels extracted from the aiMD simulations for the  $d_{\text{OH}}$  (grey solid line),  $d_{\text{OHs}}$  (blue solid line) and  $d_{\text{OHa}}$  (purple solid line) coordinates.

The time-dependent friction kernels of the  $d_{\text{OH}}$ ,  $d_{\text{OHs}}$  and  $d_{\text{OHa}}$  coordinates are compared in fig. S7, scaled by the mass of the respective coordinate. The time-dependent friction kernel of the  $d_{\text{OHa}}$  coordinate differs significantly from the one of the  $d_{\text{OHs}}$  coordinate. However, all friction kernels show various oscillating decay time scales between 10 fs and 5 ps, which is discussed in detail the main text for the example of  $d_{\text{OHs}}$ .

## XII. CONSTANT-FRICTION LINE SHAPE

The dependence of the Lorentzian line shape function eq. (S51) on the friction coefficient  $\gamma$  for the  $d_{\text{OHs}}$  coordinate is illustrated in fig. S8A and for the  $\phi_{\text{HOH}}$  coordinate in fig. S8B. A variation of  $\gamma$  does not shift the peak position but significantly changes the width. This follows analytically from the maximum of eq. (S51)

$$\frac{\partial}{\partial \omega} [\omega \tilde{\chi}''(\omega)] = \frac{L^2}{k_B T} \left[ -\frac{8\tau\omega(\omega^4\tau_\omega^4 - 1)}{(\omega^2(\tau^2 - 8\tau_\omega^2) + 4\omega^4\tau_\omega^4 + 4)^2} \right] \quad (\text{S93})$$

$$\stackrel{!}{=} 0 \quad \text{for} \quad \omega = \tau_\omega^{-1}, \quad (\text{S94})$$

which does not depend on  $\gamma$ . When considering non-harmonic effects in the potential, simulated power spectra still show no significant shifts for variation of the friction coefficient, as shown in figs. S8C and D.

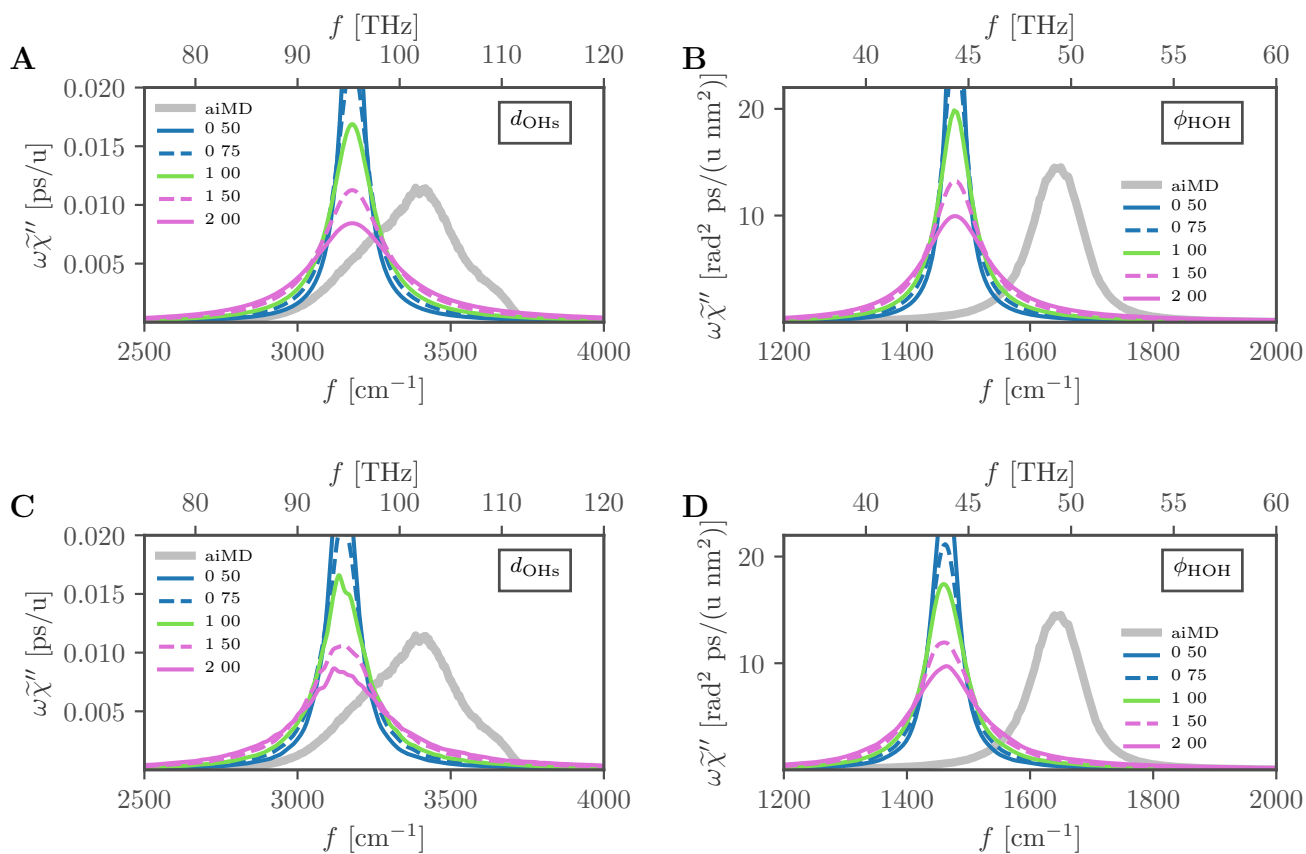


Figure S8. Power spectra, obtained from the aiMD simulations (grey solid lines) and compared to spectra from a constant friction model with the harmonic fit to the potential (A, B) and considering non-harmonic effects (C, D). The spectra are shown for variations of the friction coefficient  $\gamma_{\text{OHS}} = \Gamma'(f_{\text{OHS}})$  and  $\gamma_{\text{HOH}} = \Gamma'(f_{\text{OHS}})$ , where  $f_{\text{OHS}} = 3390 \text{ cm}^{-1}$  and  $f_{\text{HOH}} = 1650 \text{ cm}^{-1}$  are at the maxima of the respective power spectra from the simulations. **A, C:**  $d_{\text{OHs}}$  coordinate and **B, D:**  $\phi_{\text{HOH}}$  coordinate.

### XIII. SIMULATIONS OF SINGLE H<sub>2</sub>O IN THE NVE ENSEMBLE

For the aiMD simulations of single H<sub>2</sub>O molecules, representing the gas phase, 47 initial configurations were sampled from a 25 ps NVT simulation and subsequently simulated in the NVE ensemble. The NVT simulation was temperature-controlled using an individual thermostat with a time constant of 10 fs for each atom. The NVE simulations were each run for 10 ps with a time step of 0.25 fs. The distributions of their initial configurations are shown in fig. S9 to sample well the equilibrium distributions from the NVT trajectory.

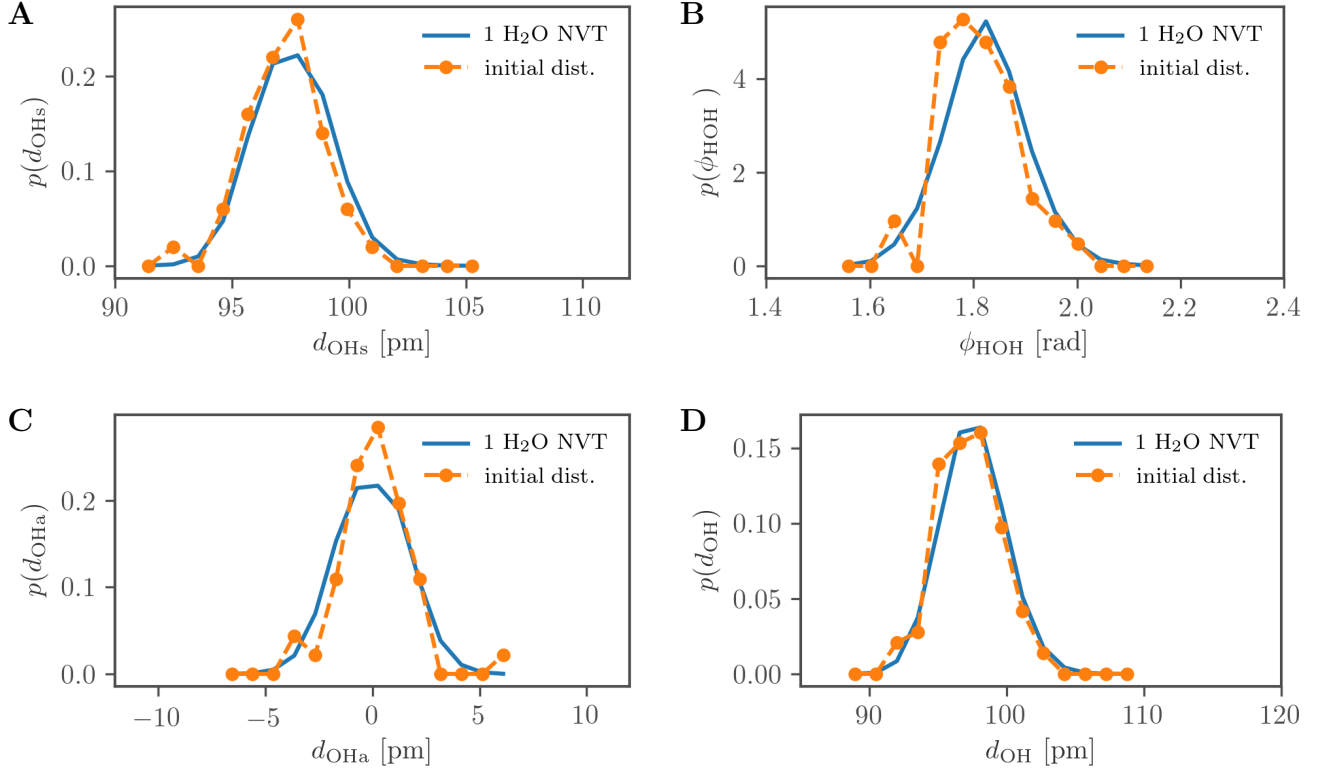


Figure S9. Comparison of the distributions for the different coordinates sampled from the aiMD simulations of a single H<sub>2</sub>O molecule under NVT conditions (blue solid lines) and 47 samples taken from the NVT trajectory as initial conditions for equivalent simulations under NVE conditions (orange dots). **A:**  $d_{\text{OH}_s}$  coordinate, **B:**  $\phi_{\text{HOH}}$  coordinate, **C:**  $d_{\text{OH}_a}$  coordinate and **D:**  $d_{\text{OH}}$  coordinate.



#### XIV. WIENER-KHINTCHINE THEOREM

The correlation function  $C_{xy}(t)$  of two stochastic processes  $x(t)$  and  $y(t)$  limited to the interval  $[0, L_t]$  is efficiently computed from the Fourier-transformed expressions  $\tilde{x}(\omega)$  and  $\tilde{y}(\omega)$  according to

$$C_{xy}(t) = \frac{1}{2\pi(L_t - t)} \int_{-\infty}^{\infty} d\omega e^{-i\omega t} \tilde{x}(\omega) \tilde{y}^*(\omega), \quad (\text{S95})$$

where the asterisk denotes the conjugate form. This is known as the Wiener-Khintchine theorem [7]. Both sides of eq. (S95) are Fourier-transformed to give

$$\int_{-\infty}^{\infty} dt e^{i\omega t} 2\pi L_t \left(1 - \frac{t}{L_t}\right) C_{xy}(t) = \tilde{x}(\omega) \tilde{y}^*(\omega), \quad (\text{S96})$$

which in the limit of large  $L_t$  reduces to

$$\tilde{C}_{xy}(\omega) = L_t^{-1} \tilde{x}(\omega) \tilde{y}^*(\omega). \quad (\text{S97})$$

Eq. (S95) can be derived starting off with the definition of the correlation function

$$C_{xy}(t) = \frac{1}{L_t - t} \int_0^{L_t - t} dt' x(t' + t) y(t'), \quad (\text{S98})$$

and making use of the convolution theorem

$$\begin{aligned} C_{xy}(t) &= \frac{1}{4\pi^2(L_t - t)} \int_0^{L_t - t} dt' \int_{-\infty}^{\infty} d\omega e^{-i\omega(t+t')} \tilde{x}(\omega) \int_{-\infty}^{\infty} d\omega' e^{-i\omega' t'} \tilde{y}(\omega') \\ &= \frac{1}{4\pi^2(L_t - t)} \int_{-\infty}^{\infty} d\omega e^{-i\omega t} \tilde{x}(\omega) \int_{-\infty}^{\infty} d\omega' \tilde{y}(\omega') \\ &\quad \int_0^{L_t - t} dt' e^{-it'(\omega + \omega')} \\ &= \frac{1}{4\pi^2(L_t - t)} \int_{-\infty}^{\infty} d\omega e^{-i\omega t} \tilde{x}(\omega) \int_{-\infty}^{\infty} d\omega' \tilde{y}(\omega') \\ &\quad 2\pi\delta(\omega + \omega') \\ &= \frac{1}{2\pi(L_t - t)} \int_{-\infty}^{\infty} d\omega e^{-i\omega t} \tilde{x}(\omega) \tilde{y}(-\omega), \end{aligned} \quad (\text{S99})$$

noting that  $\tilde{y}(-\omega) = \tilde{y}^*(\omega)$  for a real function  $y(t)$  in order to obtain eq. (S95).

- 
- [1] Kohler, F.; Findenegg, G.; Fischer, J.; Posch, H. *The Liquid State*; Verlag Chemie Weinheim, 1972.
- [2] Carlson, S.; Brüning, F. N.; Loche, P.; Bonthuis, D. J.; Netz, R. R. Exploring the Absorption Spectrum of Simulated Water from MHz to Infrared. *J. Phys. Chem. A* **2020**, *124*, 5599–5605.
- [3] Daldrop, J. O.; Kappler, J.; Brüning, F. N.; Netz, R. R. Butane dihedral angle dynamics in water is dominated by internal friction. *Proc. Natl. Acad. Sci.* **2018**, *115*, 5169–5174.
- [4] Harp, G.; Berne, B. Time-Correlation Functions, Memory Functions, and Molecular Dynamics. *Phys. Rev. A* **1970**, *2*, 975–996.
- [5] Schrader, B., Ed. *Infrared and Raman Spectroscopy: Methods and Applications*; Wiley-VCH, 1995.
- [6] Bertie, J. E.; Lan, Z. Infrared Intensities of Liquids XX: The Intensity of the OH Stretching Band of Liquid Water Revisited, and the Best Current Values of the Optical Constants of H<sub>2</sub>O(l) at 25°C between 15,000 and 1 cm<sup>-1</sup>. *Appl. Spectrosc.* **1996**, *50*, 1047–1057.
- [7] Wiener, N. Generalized Harmonic Analysis. *Acta Math.* **1930**, *55*, 117–258.